**ORIGINAL ARTICLE**

# Definition and validation of a valley amplification factor for seismic linear response of 2D homogeneous alluvial basins

Giorgio Andrea Alleanza[1] · Anna d'Onofrio[1] · Francesco Silvestri[1]

**Abstract**

The paper presents findings from a parametric study analysing geometric (e.g., shape ratio, edge inclination) and stratigraphic factors (e.g. impedance ratio) influencing ground motion in trapezoidal valleys. The study involved 2160 visco-elastic analyses, considering 180 2D models with diverse shapes and soil properties, undergoing 12 synthetic input motions. Analyses results showed that the motion at the valley centre increases with both shape and impedance ratios, while it is independent of the edge slope; on the other hand, the maximum amplification at the edges depends on their inclination and on the impedance ratio, while it is independent of the valley shape. The position and size of the zone of maximum amplification at the edges depend on all the previous parameters. A valley amplification factor (VAF) is introduced to quantify spectral acceleration increase due to 2D effects. Closed-form equations are proposed to evaluate VAF based on valley properties. The proposed VAF is then applied to predict seismic amplification in two central Italian valleys, providing results well-comparable to those obtained from 2D numerical analyses. The described approach can be easily implemented into codes of practice as a conservative design tool to estimate 2D amplification along the surface of 'shallow valleys' subjected to moderate seismic actions.

**Keywords** Seismic site response · 2D valley effects · Valley amplification factor · Visco-elastic analysis

## 1 Introduction

The historical preference for settling in alluvial valleys stems from their strategic proximity to transportation routes and waterways. However, the specific location of a settlement within the valley significantly influences its vulnerability to natural phenomena like floods,

✉ Anna d'Onofrio
donofrio@unina.it

Giorgio Andrea Alleanza
giorgioandrea.alleanza@unina.it

[1] Department of Civil, Architectural and Environmental Engineering (DICEA), University of Napoli Federico II, Naples, Italy

landslides, and earthquakes. Macroscopic observations following major earthquakes worldwide (e.g., Loma Prieta, 1989; Northridge, 1994; Kobe, 1995; Athens, 1999; Aterno Valley, 2009; Central Italy, 2016) have consistently revealed a non-uniform distribution of damage in alluvial basins. This phenomenon couldn't be fully explained by stratigraphic effects alone (Pitarka et al. 1996; Gao et al. 1996; Lanzo et al. 2011; Chiarini et al. 2011; Alleanza et al. 2019a; Pagliaroli et al. 2020).

The pioneering analytical studies by Bard and Bouchon (1980a, b) demonstrated that the intricate interaction among direct, reflected, and refracted waves results in ground motion amplification that varies significantly across the surface of an alluvial basin. This variation depends on the focalization of incoming body waves and the generation of parasitic surface waves. These surface waves can become trapped within the alluvial soil deposit due to the two-dimensional morphology of the valley and the contrast in wave propagation velocities between the bedrock and the filling soil. Consequently, this trapping induces an increase in the amplitude and duration of seismic motion. Subsequent analyses by Bard and Bouchon (1985), as well as other theoretical studies in applied seismology (e.g., Sanchez-Sesma et al. 1988; Bielak et al. 1999; Paolucci 1999) and geophysical surveys (e.g., Aki 1988) along with weak-motion records by surface arrays (e.g., Faccioli et al. 2002; De Crescenzo et al. 2018; Sgattoni et al., 2019; Sgattoni and Castellaro 2020), confirmed that irregularities may significantly modify the amplitude, duration, and frequency content of ground motion.

Despite achieving a satisfactory understanding of the main physical phenomena governing wave propagation in alluvial basins, comprehensively evaluating the quantitative influence of individual geometrical and mechanical factors remains a challenging issue (Papadimitriou 2019). Consequently, there is no clear and universally accepted methodology for simplifying the estimation of valley effects, unlike the evaluation of topographic effects.

In the literature, several studies have focused on exploring potential updates to seismic codes to incorporate valley effects in conjunction with stratigraphic amplification (e.g., Chávez-García and Faccioli 2000). Typically, a 'geometric aggravation factor' has been defined as the ratio between results obtained between 2D and 1D analyses, like the approach often adopted by codes of practice to quantify topographic amplification (e.g., Bouckovalas and Papadimitriou 2005; Pagliaroli et al. 2007). Generally, a visco-elastic model is adopted in these analyses, assuming that the geometric aggravation factor is not significantly affected by soil non-linearity, which is, however, considered in the stratigraphic amplification (see, for instance, Tropeano et al. 2018).

In recent years, numerous parametric studies have been conducted to define an appropriate valley amplification factor (VAF) (e.g., Vessia et al. 2011; Riga et al. 2016; Boudghene-Stambouli et al. 2018; Moczo et al. 2018; Kristek et al. 2018; Zhu et al. 2018a, b, c; Papadimitriou 2019; Pitilakis et al. 2019). However, a solution that adequately considers the influence of valley geometry and mechanical soil properties on the seismic response to express the variability of VAF along the valley has not been defined yet.

One of the main challenges in formulating a proper valley amplification factor is the selection of the 1D reference profile. Two possible approaches are proposed in the literature:

1. *First approach* This assumes as the reference 1D response that computed along the vertical profile corresponding to the center of the valley (e.g., Chávez-García and Faccioli 2000; Makra et al. 2005; Vessia et al. 2011; Papadimitriou 2019). While advantageous

due to reduced computational effort and clear identification of the influence of both geometrical and mechanical parameters on VAF, it may lead to an approximation at the basin edges, where the 1D reference profile can differ significantly from that corresponding to the center of the valley. This aspect is less crucial in the case of very shallow trapezoidal valley where most of the valley is characterized by a constant thickness like that at the valley centre.

2. *Second approach* This computes the VAF along the valley profile as the ratio between 2D and 1D site responses, considering the reference 1D profile varying along the valley following the valley shape (e.g., Boudghene-Stambouli et al. 2018; Moczo et al. 2018; Kristek et al. 2018; Uzielli et al. 2022). While more accurate, it involves a significant computational cost and makes it more challenging to design a simplified method for evaluating two-dimensional effects.

Following the first approach, in this study a simple to use visco-elastic Valley Amplification Factor is proposed to estimate the 2D amplification of homogeneous, symmetrical shallow valleys.

To reach this goal first an extended parametric study investigating the effects of the main factors affecting the seismic response of shallow valleys (widespread in the territories of Mediterranean countries) was carried out. The results of the numerical analyses performed on regular, simmetrical trapezoidal schemes of homogeneous alluvial valleys, assuming linear visco-elastic behavior, and adopting synthetic input signals with different characteristic frequencies, are summarised in Sects. 3 and 4. Hence, the VAF has been formulated and the individual influence of significant parameters on VAF has been evaluated and summarised in Sect. 5 where the limits of the approach are also highlighted. An analytical formulation of the VAF is then proposed that allows quantifying 2D effects on ground motion amplification along the entire valley surface, considering basin morphology, the dominant frequency of the input motion, and the mechanical properties of both alluvial soil and bedrock.

Finally, an example of an application to a real valley in Central Italy is presented in Sect. 6, comparing the VAFs obtained with complete numerical analyses and with the proposed simplified ones.

## 2 Main factors affecting 2D valley seismic response

In the literature, studies on valley effects focus on the role of factors such as:

(a)  Valley shape,
(b)  Rock/soil impedance ratio,
(c)  Bedrock slope at valley edges,
(d)  Soil inhomogeneity,
(e)  Soil nonlinearity,
(f)  Frequency content of reference motion.

The significance of valley shape was extensively explored by Bard and Bouchon (1980a, b, 1985), who defined the shape ratio (H/B) as the ratio between the maximum thickness (H) and the half-width (B) of the valley (Fig. 1).
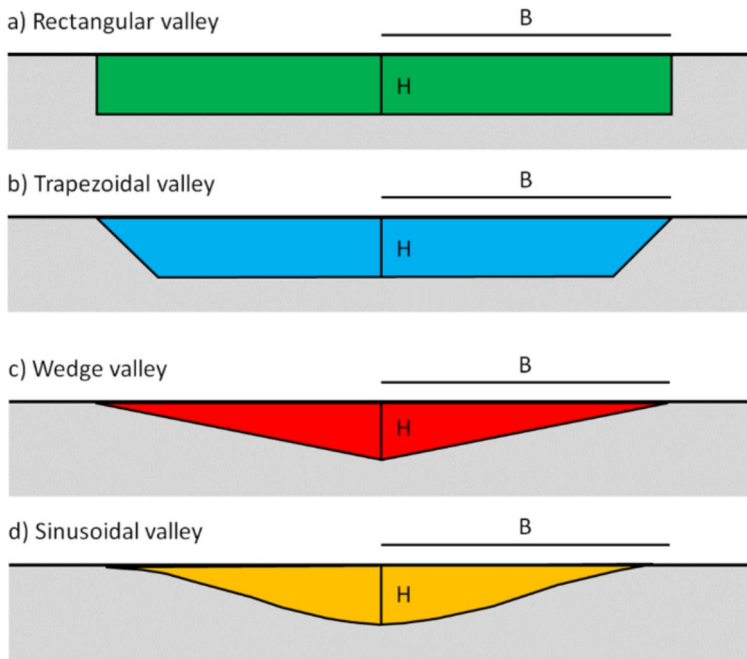
**Fig. 1** Geometrical parameters for alluvial valleys with **a** rectangular, **b** trapezoidal, **c** wedge, and **d** sinusoidal shapes

Based on the results of a series of visco-elastic numerical analyses conducted on homogeneous valleys with either a rectangular or sinusoidal shape, Bard and Bouchon (1985) observed that the two-dimensional resonance frequency, $f_{0,2D}$, surpassing that of the soil column at the centre of the valley, $f_{0,1D}$, increases with the shape ratio, $H/B$. It is important to note that the existence of a 2D resonance effect and the proportionality of the frequency to the steepness of morphological irregularities have also been demonstrated by various authors for ridges and crests (e.g., Paolucci 2002; Bray 2007), as well as for triangular-shaped embankments or dams (e.g., Dakoulas and Gazetas 1985). Bard and Bouchon (1985) provided the following relationships between the shape ratio and the resonant frequencies for the different types of waves:

$$f_{0,2D}^{P} = f_{0,1D}^{P} \cdot \sqrt{1 + \left(\frac{H}{B}\right)^2}$$
$$f_{0,2D}^{SV} = f_{0,1D}^{SV} \cdot \sqrt{1 + \left(2.9 \cdot \frac{H}{B}\right)^2} \qquad (1)$$
$$f_{0,2D}^{SH} = f_{0,1D}^{SH} \cdot \sqrt{1 + \left(2 \cdot \frac{H}{B}\right)^2}$$

where the superscripts P, SV and SH identify the corresponding compression (P) and shear waves, these latter distinguished between those inducing in-plane (SV) and out-of-plane (SH) motions.

As is well-known, even for one-dimensional propagation, the resonance frequency depends solely on the shape ratio, as well as on the wave velocity and thickness of the

deformable soil. On the other hand, the amplification at the surface is proportional to the 'impedance ratio' between the bedrock and the overlying soil, denoted as $I$. This ratio is defined as the ratio between the products of material density and propagation velocity of a given body wave. Its influence is justified by the physical refraction phenomenon, wherein seismic waves propagating upward from the bedrock encounter the interface with the alluvial deposit. At this interface, part of the energy is reflected downward, while the remaining portion is transmitted toward the basin surface. The refracted energy increases with $I$, while the reflected part (and thus, the radiation damping) decreases. Consequently, due to these mechanisms, the amplitude and duration of the surface ground motion generally increase with the impedance contrast. The above mentioned study by Bard and Bouchon (1985) lead to the definition of a 'critical shape ratio', $(H/B)_c$, defined as follows:

$$\left(\frac{H}{B}\right)_c = \frac{0.65}{\sqrt{C_v - 1}} \tag{2}$$

i.e. as a function of the ratio, $C_V$, between the shear wave velocity of the bedrock, $V_{S,BR}$, and that of the overlying soil, $V_S$. Note that the velocity ratio $(C_V)$ is a parameter less general and slightly lower than $I$, being the density ratio between rocks and soils in alluvial valleys typically variable between 1.15 and 1.50. Valleys characterized by values of $C_V$ and $H/B$ that identify a point below the threshold curve, as shown in Fig. 2, can be termed as 'shallow'. In such cases, seismic amplification at the surface is primarily due to the combination of stratigraphic one-dimensional resonance and the effect of surface waves. Conversely, if the point falls above the threshold curve, the valley is termed 'deep', and its response is governed by two-dimensional resonance.

The influence of the slope angle ($\alpha$) of the edges of a trapezoidal valley was investigated by Zhu and Thambiratnam (2016), revealing two distinct wave propagation patterns depending on its value. For high angle values (Fig. 3a), most of the ray paths of
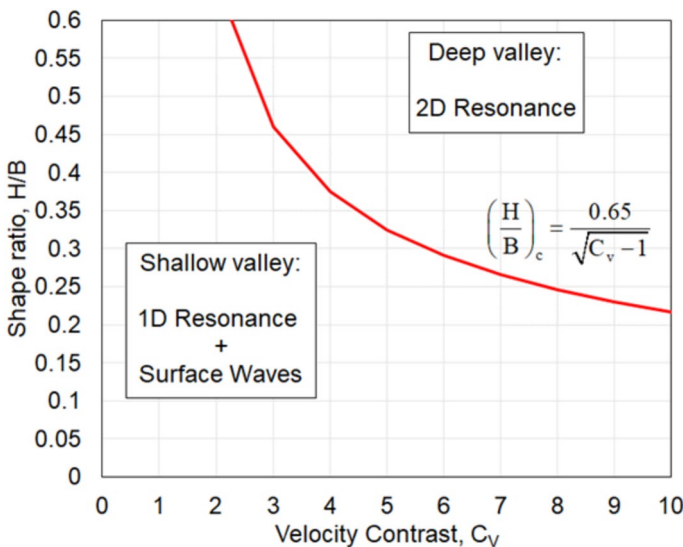


**Fig. 2** Threshold curve of the critical shape ratio vs. the velocity contrast (modified from Bard and Bouchon 1985)
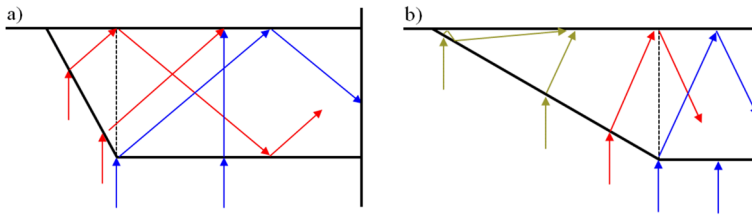
**Fig. 3** Ray paths in case of **a** high and **b** low inclination of the edge (modified from Zhu and Thambiratnam 2016)

body waves transmitted from the edges (indicated by red arrows) are directed towards the centre of the valley, where they significantly interact with the direct waves (shown by blue arrows). Conversely, for low slope inclinations (Fig. 3b), a non-negligible amount of energy becomes trapped within the edges (depicted by green arrows), leading to a substantial amplification of motion at the borders of the valley.

Typically, alluvial deposits exhibit non-homogeneity due to a shear wave velocity profile that varies with depth (d''Onofrio and Silvestri 2001), influencing the seismic response of the valley at the ground surface. A nonlinear increase in the shear wave velocity profile (*Vs*) results in amplified seismic motion compared to the homogeneous case, both at the edges and the centre of the valley (Bard and Gariel 1986). Additionally, at the valley's side, the interface between bedrock and the deformable deposit features a decreasing impedance ratio with depth, impacting the ray paths of both refracted and surface seismic waves. This, in turn, influences the position of the maximum amplification, dependent on the constructive interference between various waves, shifting it towards the valley edge (Bard and Gariel 1986).

Soil non-linearity further modifies the seismic response of the basin, as emphasized in numerous numerical literature studies (e.g., Psarropoulos et al. 2007; Gelagoti et al. 2010, 2012; Iyisan and Khanbabazadeh 2013; Riga et al. 2018; Garini et al. 2020). In one-dimensional propagation of shear waves, the strain-dependent increase in soil deformability and energy dissipation induces significant changes along the valley in terms of amplitude, frequency content, and duration of ground motion at the surface. These changes depend on the coupling between soil non-linearity and the characteristics of the reference input motion. Non-linearity often significantly affects the surface ground motion along the valley edges, particularly evident when using true nonlinear analyses with hysteretic-perfectly plastic soil models, rather than the more traditional equivalent linear approaches (see, for instance, Capatti et al. 2017).

The seismic response of alluvial valleys is also influenced by the frequency content of the incoming motion, specifically by the ratio between the mean frequency of the reference bedrock motion ($f_m$) and the resonant frequency of the valley, proportional to $f_{0,1D}$. This ratio is inversely proportional to that between the wavelength ($\lambda = V_S/f_m$) and the valley thickness, $H$. If $f_m$ is much lower than $f_{0,1D}$, the amplification is negligible because $\lambda$ is much greater than $H$, and seismic waves do not interact with the deformable layer. If $f_m$ is close to $f_{0,1D}$, the amplification is mainly due to one-dimensional resonance. Finally, if $f_m$ is greater than $f_{0,1D}$, the amplification is affected by 2D effects, resulting in greater amplification than in one-dimensional propagation (Alleanza et al. 2019b).

# 3 The numerical parametric study

An extensive series of seismic response analyses was conducted on homogeneous trapezoidal valleys (see Fig. 1b) to assess the impact of geometrical and mechanical parameters on the seismic response at the surface. The geometric characteristics of the models used are summarized in Table 1; they all share a constant thickness of 100 m and exhibit varying widths to achieve a shape ratio ranging from 0.05 to 0.25. For each H/B value, six different edge slopes were considered, ranging from 90° to the value of arctan (H/B), representing a 'wedge' geometry, which consistently corresponds to the minimum inclination.

The mechanical properties utilized in the analyses are outlined in Table 2. Both bedrock and alluvial soil were modelled as linear visco-elastic media, with a fixed shear wave velocity of 800 m/s assigned to the bedrock. The shear wave velocity of the soil deposit varied between 100 and 580 m/s. The small-strain damping ratio, $D_0$, ranged between 5 and 1% for the soil deposit and was set at 0.5% for the bedrock, resulting inversely proportional to the assigned $V_S$ for each material. The unit weight and Poisson's ratio were kept constant for each material, with values typical for alluvial soils and soft rocks.

Following the criteria established by Bard and Bouchon (1985), all analyzed models fall into the category of 'shallow valleys,' as depicted by the black dots on the chart in Fig. 4.

The resonance frequency reported in Table 2 is referred to the 1D vertical profile corresponding to the centre of the valley, and it is calculated as:

$$f_{0,1D} = \frac{V_S}{4H} \tag{3}$$

The 2D numerical simulations were conducted using the finite difference code FLAC 8.0 (Itasca Consulting Group 2016). The mesh grid consisted of quadrangular elements, with a maximum thickness set as 1/10 of the minimum propagating wavelength, following the Kuhlemeyer and Lysmer (1973) criterion, considering a maximum frequency of 20 Hz. The analysis domain (Fig. 5) was laterally extended for a length equal to one quarter of the width ($b=0.5B$, in Fig. 5), while the height of the domain was set to twice the thickness of the valley ($=H$, in Fig. 5).

Free-field boundary conditions in FLAC were simulated using one-dimensional columns, mimicking the behaviour of a laterally semi-infinite medium, connected to the mesh grid through viscous dashpots. Viscous dampers were placed at the bottom boundary, where the reference input motion was applied as a time history of shear stresses, to simulate a visco-elastic half-space. The viscous material damping was modelled using the Rayleigh formulation. Following the procedure suggested by Costanzo et al. (2019), the 'single

**Table 1** Geometrical properties

| Thickness H (m) | Width 2B (m) | Shape ratio H/B | Edge slope α (°) | Wedge slope (°) |
|---|---|---|---|---|
| 100 | 4000 | 0.05 | 90/60/45/30/15/Wedge | 2.86 |
|  | 2000 | 0.10 |  | 5.71 |
|  | 1340 | 0.15 |  | 8.53 |
|  | 1000 | 0.20 |  | 11.31 |
|  | 800 | 0.25 |  | 14.04 |

**Table 2** Mechanical properties

| Shear wave velocity | | Unit weight | | Poisson's ratio | | Damping ratio | | 1D resonance frequency $f_{0,1D}$ (Hz) | Impedance ratio $I$ | Velocity contrast $C_V$ |
|---|---|---|---|---|---|---|---|---|---|---|
| Bedrock $V_{S,r}$ (m/s) | Soil $V_S$ (m/s) | Bedrock $\gamma_r$ (kN/m³) | Soil $\gamma$ (kN/m³) | Bedrock $\nu_r$ | Soil $\nu$ | Bedrock $D_{0,r}$ (%) | Soil $D_0$ (%) | | | |
| 800 | 100 | 22 | 19 | 0.33 | 0.33 | 0.5 | 5.0 | 0.25 | 9.26 | 8.00 |
| | 130 | | | | | | 3.8 | 0.32 | 7.13 | 6.15 |
| | 180 | | | | | | 2.8 | 0.45 | 5.15 | 4.44 |
| | 270 | | | | | | 1.9 | 0.67 | 3.43 | 2.96 |
| | 360 | | | | | | 1.4 | 0.90 | 2.57 | 2.22 |
| | 580 | | | | | | 1.0 | 1.45 | 1.60 | 1.38 |
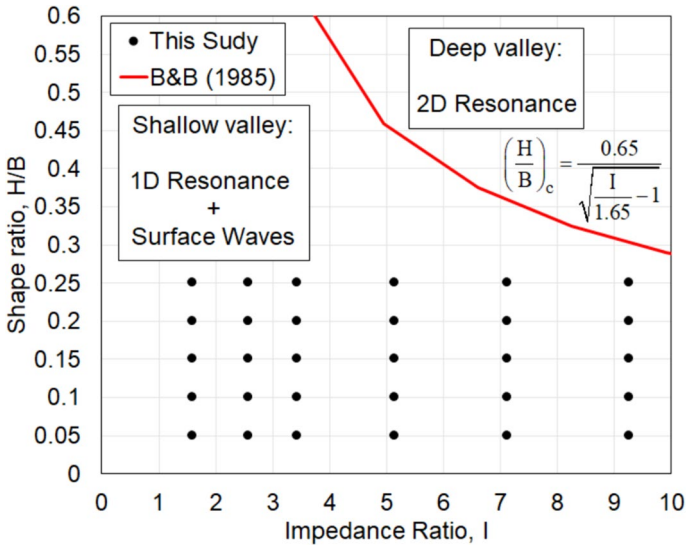
**Fig. 4** Valley schemes considered in the analysis vs. the limit curve defined by Bard and Bouchon (1985)
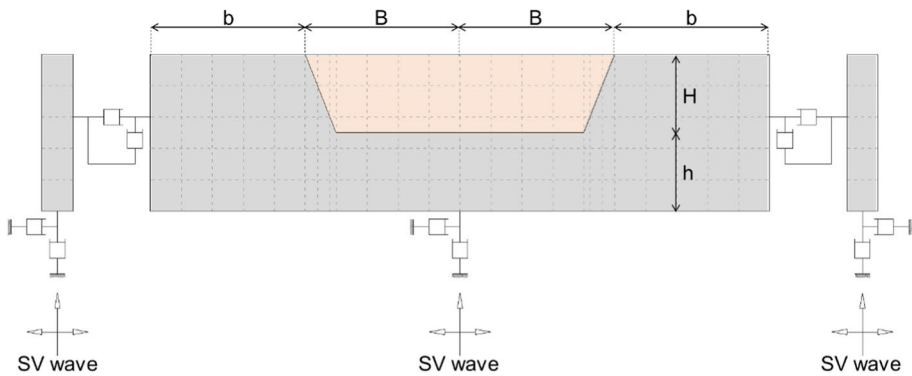


**Fig. 5** Schematic representation of the numerical model

frequency' approach implemented in the numerical code was calibrated to be equivalent to a 'double-frequency' approach. This was achieved by setting the first reference frequency equal to $f_{0,1D}$ and the second coincident with the predominant frequency of the reference input motion.

For each model, the results of 2D analyses were compared with those obtained from 1D analyses along the soil column corresponding to the centre of the valley. This comparison aimed to isolate geometric effects from stratigraphic ones. The choice of selecting the 1D response at the center of the valley as a reference was preferred to maintain a uniform reference along the valley. Additionally, shallow trapezoidal valleys are characterized by an almost constant thickness, equal to that at the centre, except for a small portion corresponding to the edges.

One-dimensional analyses were performed using the well-known code STRATA (Kottke and Rathje 2008). Given that FLAC and STRATA work in the time and frequency

domains, respectively, it was preliminarily checked that, for 1D visco-elastic analysis considering the same subsoil models in terms of boundary conditions and geometric discretization, the two codes provided consistent results, as already shown by previous comparative studies (e.g., Alleanza and Chiaradonna 2018; Verrucci et al. 2022).

The influence of the frequency content of the reference motion was analysed adopting a set of twelve Ricker wavelets as acceleration input motion, a(t), whose analytical expression is:

$$a(t) = PGA \cdot \left\{ 1 - 2 \cdot \left[ \pi \cdot f_m \cdot (t - t_0) \right]^2 \right\} \cdot e^{-\left[ \pi \cdot f_m \cdot (t - t_0) \right]^2} \tag{4}$$

with a fixed peak ground acceleration amplitude, *PGA*, equal to 0.5 g, a variable mean frequency, $f_m$, of the Fourier's spectrum, the inverse of which corresponds to half duration of the wavelet and $t_0$ the time corresponding to the PGA.

The properties of the signals are presented in Table 3, indicating the ranges of variation for both mean and predominant frequencies ($f_p$), corresponding to the peak acceleration of the response spectrum, of the seismic motion in correspondence of outcropping bedrock. The frequency ranges reported in the table are associated with different impedance ratio utilized in the study. All models in this investigation share the same valley thickness ($H = 100$ m), identical bedrock properties ($V_{s,r} = 800$ m/s and $\gamma = 22$ kN/m³), and 12 values of the ratio $\lambda_m/H$, ranging between 20 and 0.5.

Given the latter, the mean frequency of the input was derived for each value of the impedance ratio, and consequently, $f_m = V_s/\lambda_m$. For instance, for wavelet number 1, $\lambda_m/H$ is equal to 20, thus $\lambda_m$ is equal to 2000 m. Considering the range of $V_s$ in the parametric analyses between 100 and 580 m/s, the corresponding mean frequencies vary between $100/2000 = 0.05$ Hz and $580/2000 = 0.29$ Hz.

Figure 6a displays all the acceleration time histories of the input motions plotted using a normalized time variable ($t \cdot f_m$), obtained by multiplying the time, $t$, by the mean frequency of the reference input motion. In the normalized plot, accelerograms characterized by different frequency content can be compared since their shape is independent of frequency.

**Table 3** Properties of the input motions

| Wavelet # | Mean frequency $f_m$ (Hz) | Mean wavelength $\lambda_m$ (m) | Predominant Frequency $f_p$ (Hz) | $\lambda_m/H$ | $B/\lambda_m$ | $f_m / f_{0,1D}$ | $T_m / T_{0,1D}$ |
|---|---|---|---|---|---|---|---|
| 1 | 0.05–0.29 | 2000.00 | 0.06–0.37 | 20.00 | 1.00 | 0.20 | 5.00 |
| 2 | 0.10–0.58 | 1000.00 | 0.13–0.74 | 10.00 | 2.00 | 0.40 | 2.50 |
| 3 | 0.11–0.64 | 900.00 | 0.14–0.82 | 9.00 | 2.20 | 0.45 | 2.25 |
| 4 | 0.13–0.73 | 800.00 | 0.17–0.93 | 8.00 | 2.50 | 0.50 | 2.00 |
| 5 | 0.14–0.83 | 700.00 | 0.18–1.06 | 7.00 | 2.90 | 0.58 | 1.75 |
| 6 | 0.17–0.97 | 600.00 | 0.22–1.23 | 6.00 | 3.30 | 0.67 | 1.50 |
| 7 | 0.20–1.16 | 500.00 | 0.26–1.49 | 5.00 | 4.00 | 0.80 | 1.25 |
| 8 | 0.25–1.45 | 400.00 | 0.32–1.85 | 4.00 | 5.00 | 1.00 | 1.00 |
| 9 | 0.33–1.93 | 300.00 | 0.42–2.50 | 3.00 | 6.70 | 1.30 | 0.75 |
| 10 | 0.50–2.90 | 200.00 | 0.64–3.70 | 2.00 | 10.00 | 2.00 | 0.50 |
| 11 | 1.00–5.80 | 100.00 | 1.28–7.14 | 1.00 | 20.00 | 4.00 | 0.25 |
| 12 | 2.00–11.60 | 50.00 | 2.56–14.30 | 0.50 | 40.00 | 8.00 | 0.12 |
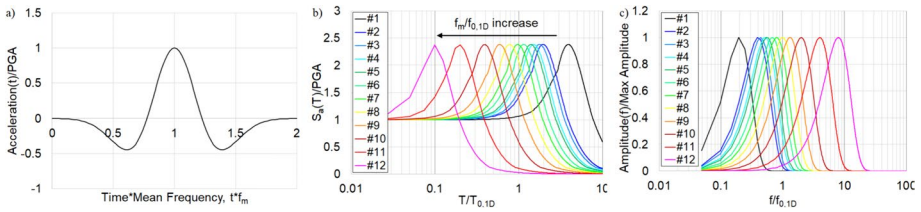
**Fig. 6** Reference input motions: **a** shape of accelerogram; **b** response spectra; **c** Fourier's spectra

Figure 6b and c present the acceleration response spectra and the Fourier spectra of the input motions, respectively. Normalized plots are also used in these cases: the spectral acceleration, $S_a(T)$, in Fig. 6b is divided by the peak ground acceleration, PGA, while the amplitudes of each Fourier spectrum are normalized by the relevant maximum value. Additionally, the period and frequency are divided by the respective one-dimensional resonance values, $T_{0,1D}$ and $f_{0,1D}$. The use of wavelets as reference input motions facilitates a detailed analysis of ground motions by identifying direct, indirect, and surface waves, allowing for easier tracking of ray paths within the valley.

A wide frequency range has been investigated, with accelerograms that can be representative of both impulsive sources (c.f. Fig. 6c #9–12) and signals with a wider frequency content (c.f. Fig. 6c #1–3).

## 4 The influence of different factors

By combining 30 geometrical models (5 valley shape factors multiplied by 6 slope angles, as listed in Table 1) with 6 shear wave velocity values (as outlined in Table 2) and 12 input motions (as detailed in Table 3), a total of 2160 two-dimensional analyses were conducted. In contrast, the reference one-dimensional analyses amounted to 72, considering that the soil thickness at the centre of the analyzed models is constant and equal to 100 m.

The results of the parametric analyses were initially presented in terms of time histories of acceleration at the surface, allowing a comparison between the outcomes obtained from 2D and 1D analyses. Furthermore, to emphasize the influence of subsurface morphology on surface amplification, the same results were then synthesized in terms of spectral amplification, A:

$$A\left(T, \frac{x}{B}\right) = \frac{S_{a,s}\left(T, \frac{x}{B}\right)}{S_{a,r}(T)} \tag{5}$$

with:

- $S_{a,s}\left(T, \frac{x}{B}\right)$: spectral acceleration of ground motion at the surface computed at a distance x from the centre of the valley
- $S_{a,r}(T)$: spectral acceleration of the reference input motion
- $\frac{x}{B}$: normalized abscissa representing the ratio between the distance from the centre, x, and the half-width of the basin, B,

and finally, a 'geometrical aggravation factor' was computed as:

$$AG_{2D/1D}\left(T, \frac{x}{B}\right) = \frac{A_{2D}\left(T, \frac{x}{B}\right)}{A_{1D}(T, 0)} \qquad (6)$$

being $A_{2D}$ and $A_{1D}$ the amplification factors obtained with 2D and 1D analyses, respectively. Note that $AG_{2D/1D}$ is the same aggravation factor as defined by Chávez-García and Faccioli (2000). Indeed, $A_{1D}$ and $A_{2D}$ are calculated as the ratio of the 1D or 2D spectra at the surface and at the bedrock, and thus $AG_{2D/1D}$ is simply the ratio between the 2D and 1D surface spectra.

In the following, a synthesis of the numerical results is reported with the aim of highlighting the influence of the single geometrical and mechanical properties on the 2D amplification at surface. For each of the analysed factors, some typical and most significant results are shown. All the details on the results of the parametric analysis can be found in Alleanza (2022).

## 4.1 Influence of shape ratio

The influence of the shape ratio, *H/B*, on the seismic response can be illustrated through Fig. 7, which compares the time histories of the horizontal and vertical components of the acceleration at the surface. This comparison is made for two valley schemes characterized by the same impedance ratio ($I=9.26$) and edge slope ($\alpha=45°$), but with two different shape ratios: one equal to 0.05 (Fig. 7c–e) and the other to 0.25 (Fig. 7d–f). The models were subjected to the same input motion #10 (Fig. 7a), ensuring that the frequency ratio, $f_m/f_{0,1D}$, was equal to 2 in both cases. The time history of the 1D response at the surface obtained along the profile corresponding to the centre of both valleys is reported in Fig. 7b.
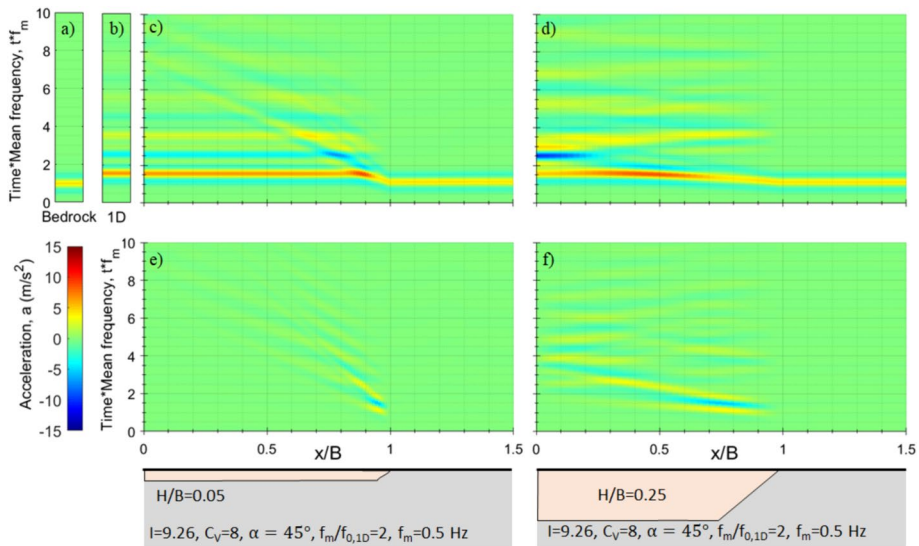


**Fig. 7** Influence of shape ratio—Horizontal accelerograms: **a** input motion, **b** computed at the surface of the 1D soil column at the centre of the valley, and along the surface of the valleys with **c** H/B=0.05 and **d** H/B=0.25. Vertical accelerograms computed along the surface of the valleys with **e** H/B=0.05 and **f** H/B=0.25

The contour plots in this figure, as well as those in the following, are drawn using a normalized abscissa, $x/B$, representing the ratio between the distance from the centre, $x$, and the half-width of the basin, $B$, while the ordinate is the normalized time, as defined in Sect. 2.

In the central zone of the flat basin (Fig. 7c), the peak motion amplitudes of the horizontal components closely resemble those of the one-dimensional soil column (Fig. 7b), aiding in identifying the first and subsequent arrivals of the upcoming direct and reflected shear waves. The interference of body waves with the surface waves generated from the valley edge and propagating within the basin can be clearly identified by the inclined fringes, forming a sort of 'dromochrone' with a slope approximately equal to the Rayleigh wave velocity. However, in this specific case with the lowest shape ratio ($H/B = 0.05$), they only affect the surface ground motion in a limited zone close to the edges; elsewhere, the horizontal acceleration is similar to that obtained by 1D analysis at the centre of the valley (Fig. 7b).

Conversely, for the highest value of the shape ratio, $H/B = 0.25$ (Fig. 7d), the seismic motion at the ground surface is significantly influenced by the propagation of Rayleigh waves and their interference with direct and reflected waves along the entire basin. The response is different from the 1D case everywhere in the valley, including the central zone where the positive peak amplitude is reduced, and a negative peak appears due to the interference. As confirmed by the response of valley models with intermediate values of the shape ratio (Alleanza 2022), the value of the peak ground acceleration near the edge is not influenced by H/B, while its relative position x/B varies, approaching the center of the valley as the shape ratio increases.

On the other hand, if the absolute position is considered, the abscissas of the maximum acceleration are located at the same distance from the edge, confirming the findings by Zhu and Thambiratnam (2016), based on the geometry of the interference of wave paths. For edge slopes greater than 30°, the zone of maximum interference between the direct, reflected, and refracted waves falls outside that corresponding to the inclined edges and extends for a length equal to $H \cdot \tan(\alpha)$ (Zhu and Thambiratnam 2016). Hence, the zone of the valley affected by the two-dimensional amplification phenomena increases with the shape ratio, extending from the edges towards the centre.

These trends are also reflected in the vertical accelerations at the surface, which are barely perceptible at the edge of the valley for the lowest H/B (Fig. 7e), while they attain a magnitude comparable to the horizontal component at the centre of the valley with $H/B = 0.25$ (Fig. 7f). The above results also show that for a high shape ratio, the response is characterized by a marked asynchronism of the seismic motion along the basin, which should be accounted for in the analysis of particularly extensive infrastructures crossing such kinds of valleys, e.g., dams or embankments, pipelines, bridges (see, for instance, Capatti et al. 2017). In the case of very shallow valleys, instead, the motion is in-phase along most of the basin, except for the zone near the edges.

The results of the same analyses are also represented in Fig. 8, in terms of the amplification function (i.e., the ratio between the Fourier spectra of acceleration at the surface and at bedrock), computed at the ground surface of the 1D profile corresponding to the centre of the valley (Fig. 8a), as well as along the basins characterized by $H/B = 0.05$ (Fig. 8b) and $H/B = 0.25$ (Fig. 8c). The frequencies are normalized with respect to $f_{0,1D}$, i.e., the fundamental frequency of the 1D profile corresponding to the centre of the valley.

The results confirm what has been already observed in terms of acceleration time histories. In the case of $H/B = 0.05$ (Fig. 8b), the amplification function computed within the central part of the valley is very similar to that of the 1D profile (Fig. 8a), with the
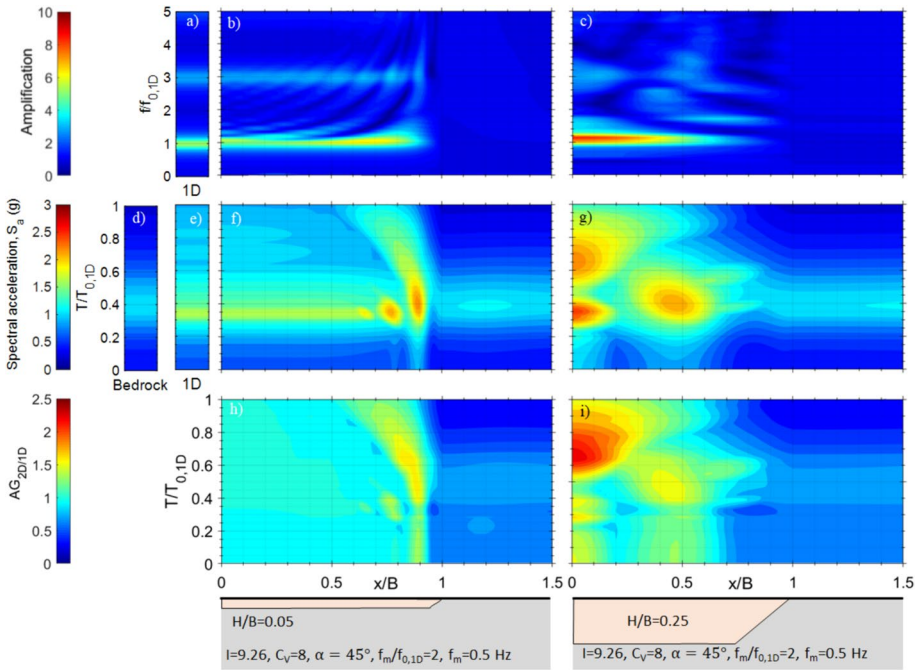
**Fig. 8** Influence of shape ratio—Amplification function for **a** 1D soil column, valleys with **b** H/B = 0.05 and **c** H/B = 0.25. Acceleration response spectra for: **d** input motion, **e** 1D soil column, valleys with **f** H/B = 0.05 and **g** H/B = 0.25. Geometrical aggravation factor $AG_{2D/1D}$ for valleys with **h** H/B = 0.05 and **i** H/B = 0.25

fundamental frequency equal to $f_{0,1D}$ and a secondary peak at about 3 times this value, while towards the edge, the fundamental frequency shows a slight increase. On the other hand, the amplification function of the valley with H/B = 0.25 (Fig. 8c) is characterized by a 2D resonance frequency, $f_{0,2D}$, equal to 1.1–1.2 $f_{0,1D}$ in the central area and of the order of 1.8–2 $f_{0,1D}$ at the edge.

To evaluate the aggravation factor, $AG_{2D/1D}$, as defined by Eq. (6), the data have been first synthesized in terms of response spectra. Figure 8f and g show the response spectra obtained along the two valleys, while Fig. 8d and e respectively report the spectral acceleration of the input motion and at the surface of the 1D reference profile at the valley centre. The periods are normalized with respect to the resonance period of the reference soil column, $T_{0,1D}$. The spectral amplitudes are represented up to $T/T_{0,1D} = 1$, because for higher values, no significant 2D amplification effects have been observed, as discussed in detail in the follow. (see also Vessia et al. 2011).

In accordance with the previous observations, the spectral response of the valley with $H/B = 0.05$ (Fig. 8f) is close to that of the 1D column all along the valley, except for the edge zone. The maximum spectral accelerations correspond to a period next to the predominant period of the input motion (Fig. 8d), both at the centre and at the edge of the valley. A further peak amplification at higher periods can be detected at the edge of the valley ($x/B = 0.90 - 0.95$) due to Rayleigh waves.

On the other hand, for the basin characterized by $H/B = 0.25$ (Fig. 8g), a marked spatial variability of the spectral response can be observed. At the centre of the valley,

the maximum amplification occurs both close to the predominant period ($T/T_{0,1D}=0.35$) and for longer periods ($T/T_{0,1D}=0.6-0.7$), probably due to the 2D resonance of the valley.

The previous results are represented in terms of aggravation factor in Fig. 8h and i, respectively for the two shape ratios selected. In agreement with what was observed above, for $H/B=0.05$, the aggravation factor is almost unitary in the central zone and moderately increases towards the edge due to 2D effects (Fig. 8h). For $H/B=0.25$, instead, $AG_{2D/1D}$ is significantly greater than unity in both the central and the lateral zones (Fig. 8i), confirming that for high shape ratios (although still lower than the critical value defined by Eq. 1) even the surface amplification of a so-called 'shallow valley' is substantially influenced by 2D effects.

The choice of considering only the periods lower than $T_{0,1D}$ has been borrowed from previous literature results e.g. Vessia et al. (2011) and Papadimitriou et al. (2018). It is further justified by the results of the numerical analyses shown in Figs. 9, 10 and 11, where the response spectra computed by 2D analyses at three representative normalised abscissae (x/B=0, x/B=0.5, x/B=0.95) along the very shallow (H/B=0.05) and shallow valley (H/B=0.25), are compared to those evaluated at the centre of the valley by 1D analysis and to that of the input motion. In the same figures the amplification factors $AG_{1D}$ and $AG_{2D}$, as well as their ratio, $AG_{2D/1D}$, are also reported.

As already observed, in the case of the very shallow valley (H/B=0.05) 2D effects become significant at the edge of the valley. For this reason, the ratio $AG_{2D/1D}$ is equal to unity both at the centre (Fig. 9a, c) and at x/B=0.5 (Fig. 10a, c), whatever the period
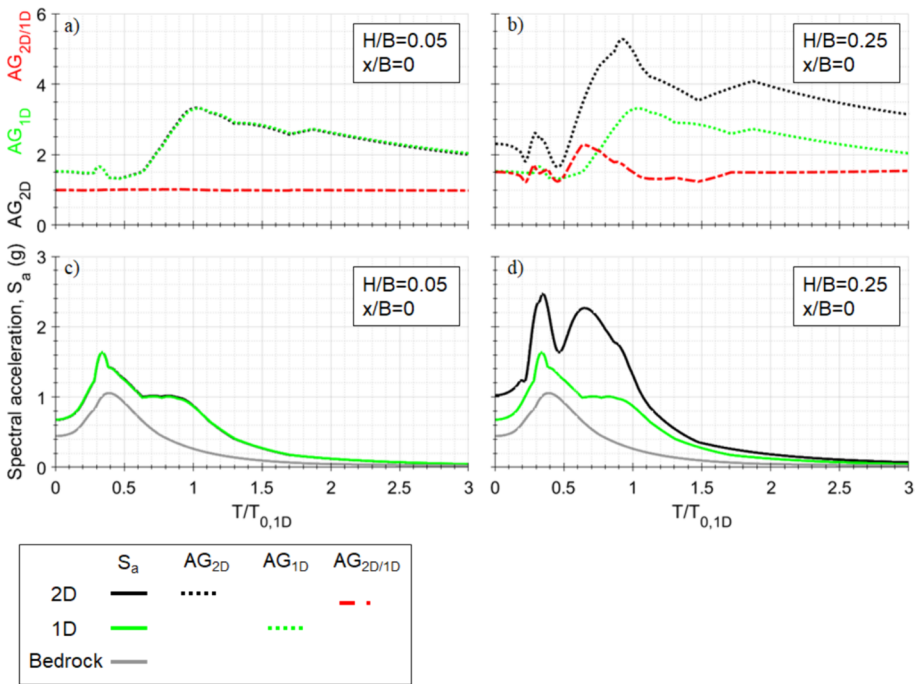


**Fig. 9** Comparison between the acceleration response spectra (**c**, **d**), AG and $AG_{2D/1D}$ (**a**, **b**) obtained at centre of the valley with 2D (black lines), 1D (green lines) analyses, for H/B=0.05 and 0.25
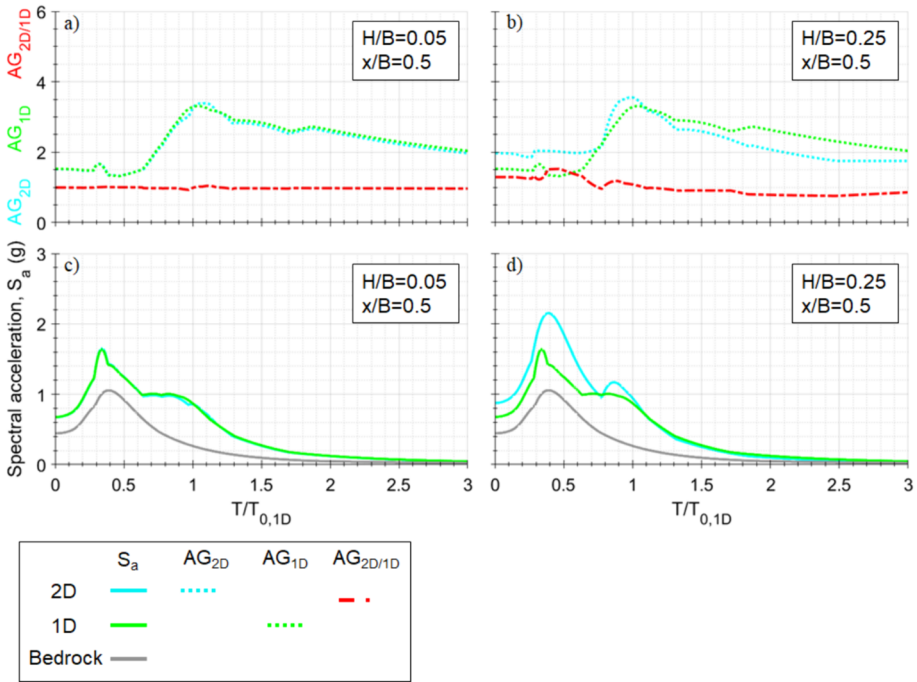
**Fig. 10** Comparison between the acceleration response spectra (**c**, **d**), AG and $AG_{2D/1D}$ (**a**, **b**) obtained at x/B = 0.5 with 2D (cyan lines), 1D (green lines) analyses, for H/B = 0.05 and 0.25

considered. Near the edge (Fig. 11a, c), instead, the 2D spectral acceleration is always lower than that of 1D analyses, thus $AG_{2D/1D}$ is lower than 1.

In the case of H/B = 0.25, the 2D spectral acceleration at the centre of the valley (Fig. 9b, d) is higher than that computed by 1D analysis for periods lower than $T_{0,1D}$, while for longer periods the difference between the two spectra is almost negligible.

Moving from the centre of the valley towards the edge, for x/B = 0.5 (Fig. 10b, d) the spectral response is mainly ruled by the predominant period of the input motion, and the 2D spectral acceleration is greater than that relevant to 1D propagation for periods close to the predominant one ($T/T_{0,1D}$ = 0.4). Moreover, for periods greater than $T_{0,1D}$ the 2D spectral ordinates are slightly lower than the corresponding 1D values, hence $AG_{2D/1D}$ is greater than unity for $T/T_{0,1D}$ < 1. Therefore, the 2D effects influence the spectral response for periods shorter than the 1D resonance period, while they become negligible at longer periods.

Finally, for x/B = 0.95 and H/B = 0.25 (Fig. 11b, d), the 2D response is always smaller than the 1D response.

Finally, as expected, the shape ratio also influences the value of the 2D resonance frequency calculated at the centre of the valley. Figure 12 summarizes all the results obtained in this study in terms of ratio $f_{0,2D}/f_{0,1D}$ as a function of H/B, distinguishing by blue and red symbols the results obtained for trapezoidal and wedge valley shapes, respectively. It is apparent that $f_{0,2D}$ always increases with H/B, significantly, depending on the geometry of the valley. As a matter of fact, the values of $f_{0,2D}$ computed in this
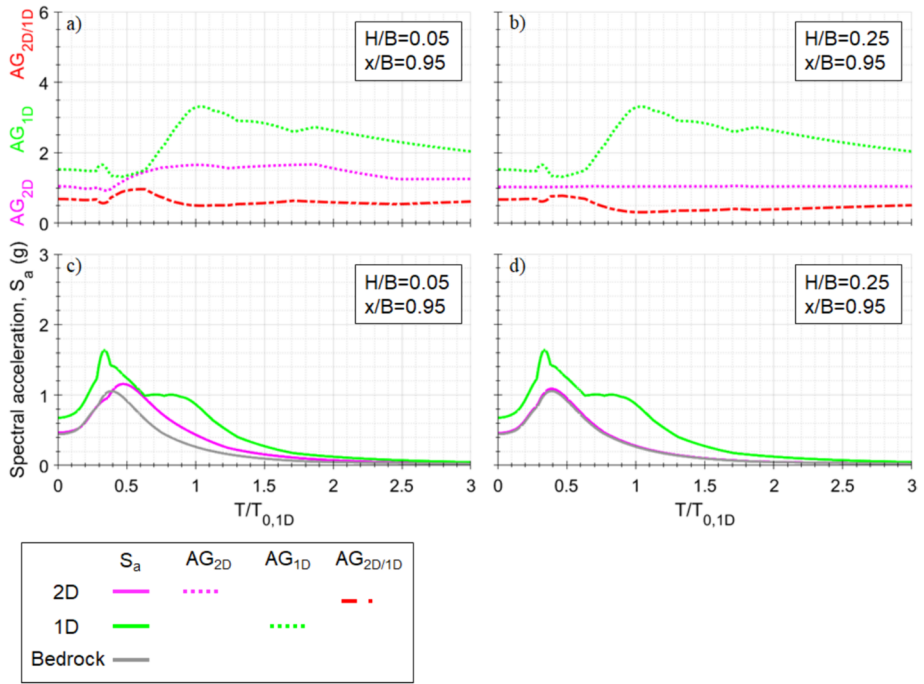
**Fig. 11** Comparison between the acceleration response spectra (**c, d**), AG and $AG_{2D/1D}$ (**a, b**) obtained at x/B = 0.95 with 2D (magenta lines), 1D (green lines) analysis for H/B = 0.05 and 0.25



**Fig. 12** Comparison between the values of $f_{0,2D}/f_{0,1D}$ obtained in this study for trapezoidal (blue circles) and wedge (red diamonds) geometries and the curves suggested by Bard and Bouchon (1985) for sinusoidal (yellow line and triangles) and rectangular (green line) shapes
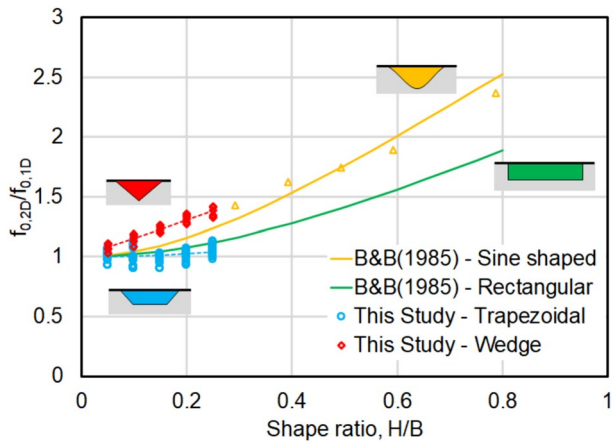
study for wedge-shaped valleys are almost similar to those obtained by Bard and Bouchon (1985) for sinusoidal valleys (yellow triangles and curve), and they result higher than those calculated for trapezoidal basins, which in turn are in good agreement with those obtained by Bard and Bouchon (1985) for rectangular valleys.

## 4.2 Influence of impedance ratio

The role of impedance ratio on two-dimensional seismic amplification at the surface was investigated by assigning five different shear velocity values (listed in Table 2) to the homogeneous soil deposit laying on bedrock characterized by a constant shear wave velocity of 800 m/s. Hereafter, the response obtained applying the same input motion to valleys characterized by the same geometrical shape (H/B = 0.25, α = 45°) and by two different impedance ratios (I = 1.60 and 9.26) is compared as a reference example. Figure 13 shows the horizontal and vertical acceleration computed for both valleys. As expected, the amplification and the duration of seismic motion are strongly influenced by the impedance ratio: the energy transmitted at the edge interface and the amplitude of the generated Rayleigh waves increase with the impedance ratio. In the case of stiff alluvial soil (I = 1.6), the horizontal acceleration is poorly amplified (Fig. 13b, c), and the vertical accelerations are negligible (Fig. 13g) along the whole valley. Instead, in the case of the valley filled with soft soil (I = 9.26), 2D amplification and significant vertical motion can be clearly detected (Fig. 13f, h), as already observed in the previous subsection (see Fig. 7c, d).

The amplification functions along the valley characterized by a low impedance ratio (Fig. 14a, b) are almost constant and do not show any significant peaks. Thus, the 2D effects are negligible for most of the valley, notwithstanding the relatively high shape ratio equal to 0.25. These trends are confirmed by the 2D spectral accelerations (Fig. 14g) that are comparable to those of the 1D column (Fig. 14f); both are poorly affected by the propagation, as observed by comparing the results reported in Fig. 14e, f, and g. Therefore, the aggravation factor, $AG_{2D/1D}$ (Fig. 14m), is almost equal to 1 throughout the entire valley, and thus no appreciable 2D effects can be detected in the case of a low impedance ratio, whereas they are significant for the more deformable basin, as discussed previously (§4.1). This confirms that the seismic response of alluvial valleys is governed by the combination of shape and impedance ratios, rather than by the values assumed by a single parameter (Bard and Bouchon 1980a,b, 1985).
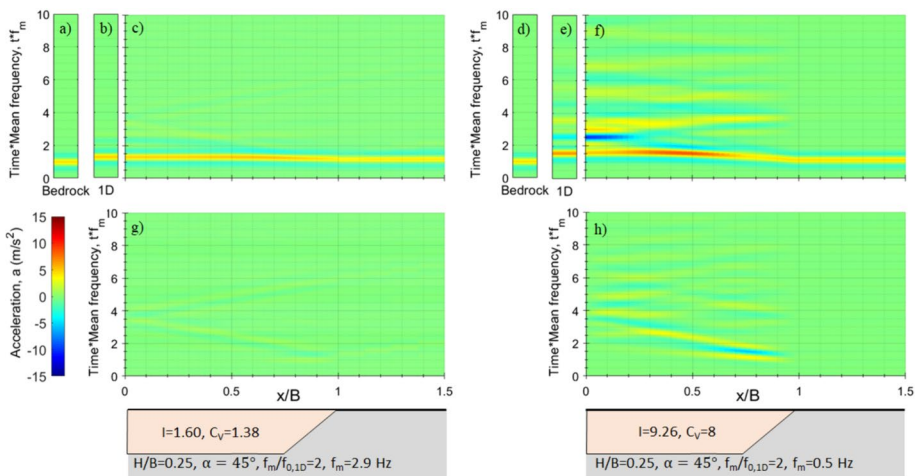


**Fig. 13** Influence of impedance ratio—Horizontal accelerograms: **a, d** input motion, **b, e** computed at the surface of the 1D column at the centre of the valley, and along the surface of the valleys with **c** I = 1.60 and **f** I = 9.26. Vertical accelerograms computed along the surface of the valleys with **g** I = 1.60 and **h** I = 9.26
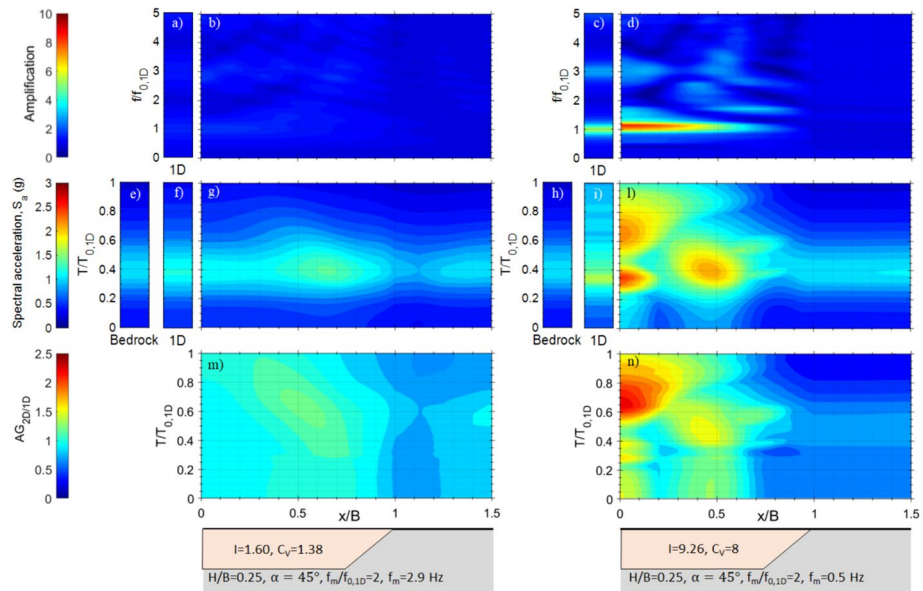
**Fig. 14** Influence of impedance ratio—Ratio between Fourier spectra at the surface and the bedrock computed by **a**, **c** 1D analysis at the centre of the valley, **b**, **d** 2D analyses along the valley profile. Acceleration response spectra: **e**, **h** input motion; **f**, **i** computed by 1D analysis at the surface of the column at the centre of the valley; **g**, **l** computed by 2D analyses along the valley surface. Aggravation factor, $AG_{2D/1D}$, for **m** I = 1.60 and **n** I = 9.26

## 4.3 Influence of the edge slope

To assess the impact of the edge slope, six different angles were considered in the analyses, ranging from 90° to the value corresponding to the wedge shape (i.e., arctan H/B). To better illustrate this effect, the behaviour of two valleys with the same mechanical properties and shape ratio, but with edge slopes ($\alpha$) of 90° and 45°, respectively, will be compared. The 2D horizontal accelerations computed for both slope angles (Fig. 15c, d) at the valley centre are comparable to those computed by the 1D analysis (Fig. 15b), indicating that the response in the middle of the valley is not significantly affected by the edge slope.

A different behaviour can be observed at the edge, where the abscissa of the maximum acceleration shifts towards the centre as the slope angle decreases. This is highlighted in Fig. 15a and b, where the red arrows indicate the positions of the maximum accelerations, as seen in the case of $\alpha = 90°$ where x/B = 0.55, while in the other case x/B = 0.45. The time history of the vertical component of the acceleration for a given impedance ratio, I (Fig. 15e, f), shows that the direction of transmitted waves, and consequently, the location of maximum interaction between the direct and the Rayleigh waves, depends on the slope angle. The maximum accelerations occur at x/B = 0.85 for $\alpha = 90°$ and at x/B = 0.75 in the other case.

The amplification functions (Fig. 16b, c) reveal that the slope angle influences the peak at the first resonance frequency less significantly than those relevant to the higher modes. This effect is confirmed by the response spectra, which for $\alpha = 90°$ appear
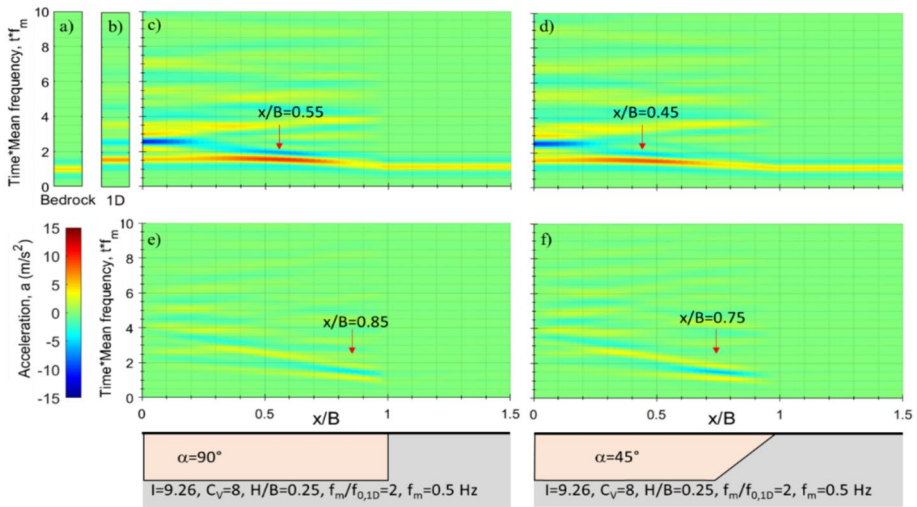
**Fig. 15** Influence of slope edge—Horizontal accelerograms: **a** input motion; computed at the surface for **b** 1D response at the valley centre; 2D analyses for **c** α=90° and **d** α=45°. Vertical acceleration for **e** α=90° and **f** α=45°
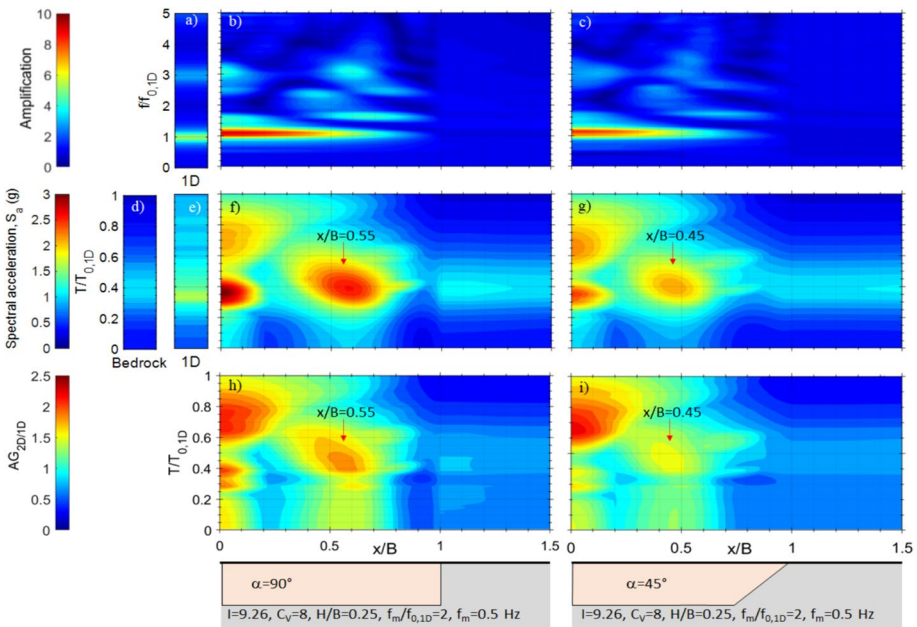


**Fig. 16** Influence of slope edge—Ratio between Fourier spectra at the surface and bedrock for **a** 1D analysis and 2D analyses for **b** α=90° and **c** α=45°. Acceleration response spectra for: **d** input motion; **e** 1D analysis; 2D analyses for **f** α=90° and **g** α=45°. Aggravation factor, AG$_{2D/1D}$, for **h** α=90° and **i** α=45°

slightly higher both at the centre and towards the edge (Fig. 16f–g). This influence is reflected even more apparent by the aggravation factor (Fig. 16h, i).

### 4.4 Influence of frequency of the input motion

To emphasize the effect of the frequency content of the incoming motion, three different cases will be examined hereafter, with $f_m$ significantly lower, close to, and higher than $f_{0,1D}$, respectively.

In the case of $f_m/f_{0,1D}=0.2$ (i.e., $f_m << f_{0,1D}$), which corresponds to $\lambda_m/H=20$ (i.e., $\lambda >> H$), regardless of the valley shape and the impedance ratio (i.e., H/B, I, $\alpha$), the motion along the surface is not influenced by the presence of the soil. In other words, the accelerations (Fig. 17b, c) and the spectra (Fig. 17e, f) obtained with 1D and 2D analyses are equal to those of the input motion (Fig. 17a, d). This is further confirmed by the absence of any parasitic vertical motion (Fig. 17g) and by the aggravation factor $AG_{2D/1D}$ (Fig. 17h), which is equal to unity throughout the entire basin and for all periods.

The surface motion along the valley becomes comparable to the 1D response as the frequency $f_m$ increases, approaching $f_{0,1D}$. Figure 18 depicts the $AG_{2D/1D}$ calculated for H/B=0.05 (left plots) and 0.25 (right plots) as the mean frequency varies up to $f_{0,1D}$. For $f_m/f_{0,1D}=0.58$ (Fig. 18a, b), regardless of the valley shape, the 2D amplification is not significantly different from the 1D response. As the frequency increases, for the shallowest valley (H/B=0.05), the aggravation factor $AG_{2D/1D}$ is at most equal to 1.1 for $f_m=f_{0,1D}$ (Fig. 18c, e, g). Conversely, for H/B=0.25, a two-dimensional amplification can be observed already for $f_m/f_{0,1D}=0.67$ (Fig. 18d), and for $f_m$ close to $f_{0,1D}$ (Fig. 18f, h), $AG_{2D/1D}$ is at most equal to 1.6–1.7. However, results related to lower impedance ratios, e.g., $I=3.43$, indicate that even for H/B=0.25, the aggravation factor $AG_{2D/1D}$ is at most 1.1–1.2 for $f_m=f_{0,1D}$ (Alleanza 2022). This is because, for high impedance contrast, the shape ratio H/B=0.25 is close to the critical value defined by Bard and Bouchon (1985), which identifies the transition from 'shallow' to
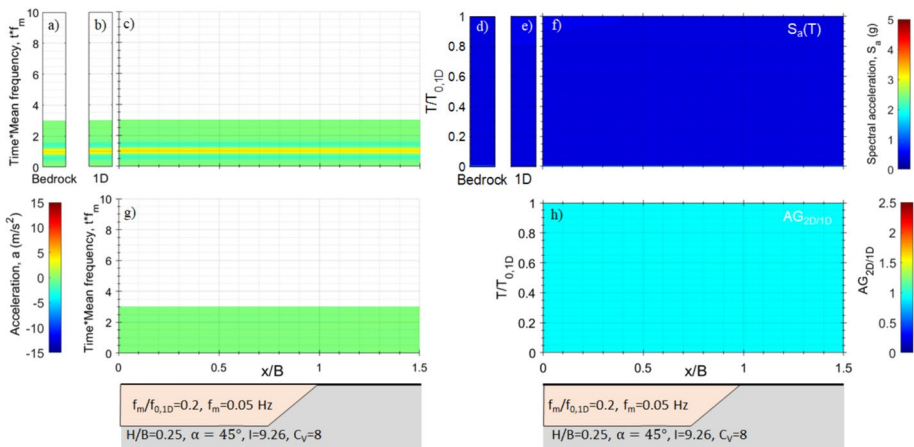


**Fig. 17** Influence of the frequency of the input motion—Horizontal accelerograms for **a** input motion and at the surface for **b** 1D analysis, **c** 2D analysis and **g** vertical acceleration for $f_m/f_{0,1D}=0.2$. Acceleration response spectra for **d** Input motion; **e** 1D analysis; **f** 2D analysis **h** $AG_{2D/1D}$ for $f_m/f_{0,1D}=0.2$
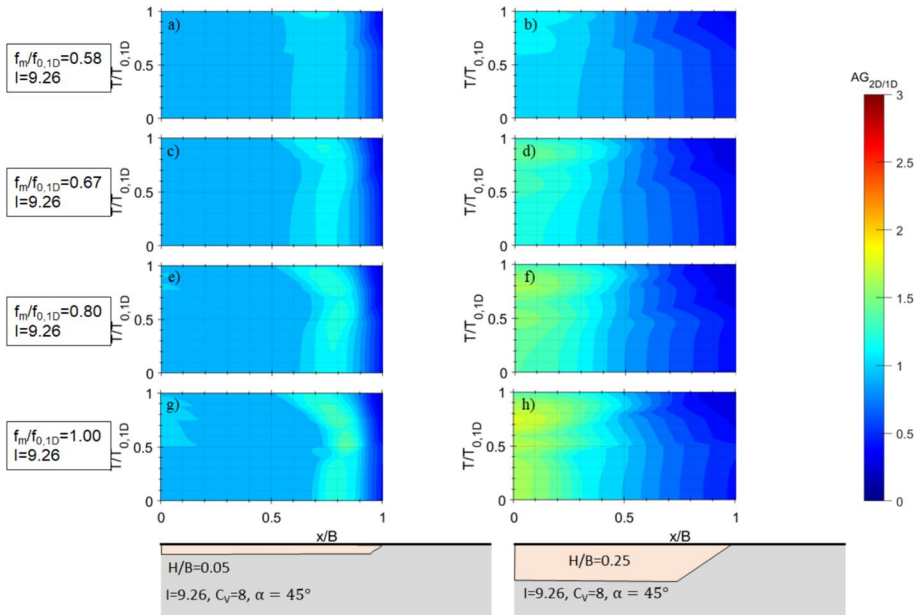
**Fig. 18** Influence of the frequency of–the input motion—$AG_{2D/1D}$ for I=9.26, H/B=0.05 and $f_m/f_{0,1D}$ equal to **a** 0.58, **c** 0.67, **e** 0.80, **g** 1.00. $AG_{2D/1D}$ for I=9.26, H/B=0.25 and $f_m/f_{0,1D}$ equal to **b** 0.58, **d** 0.67, **f** 0.80, **h** 1.00

'deep' valleys. Therefore, in this case, a 2D resonance mechanism is likely to occur, characterized by higher amplification in the centre of the valley compared to the edges (Bard and Bouchon 1985).

Finally, if $f_m > f_{0,1D}$, two-dimensional effects predominate over one-dimensional response, and the aggravation factor $AG_{2D/1D}$ is significantly greater than unity, increasing with $f_m$, as shown in the previous sections.

To verify the effectiveness of the normalised parameters adopted and the generality and sufficiency of the performed analyses, a further set of analyses was carried out considering a reduced valley thickness, H, of 30 m keeping the shape ratio equal to 0.25. All the domain dimensions have been consequently adjusted to guarantee the optimization of the numerical model. The analyses were carried out modelling the deformable soil as a homogeneous visco-elastic material and adopting a reference input motion that ensured a value of frequency ratio, $f_m/f_{0,1D}$, equal to that adopted in the previous set of numerical analyses. The results obtained adopting the reduced geometrical model were then compared to those obtained in the previous set of analyses in terms of $AG_{2D/1D}$.

As an example, the contours of $AG_{2D/1D}$, computed for both thicknesses and for $f_m/f_{0,1D}$ equal to 1 and 2 are plotted in Fig. 19a–d, respectively. They show that the model response is independent of the individual values of H, B, x and $f_m$, if the dimensionless variables H/B, $f_m/f_{0,1D}$ and x/B are the same, thus confirming the validity of the dimensionless variables adopted in the parametric analyses.
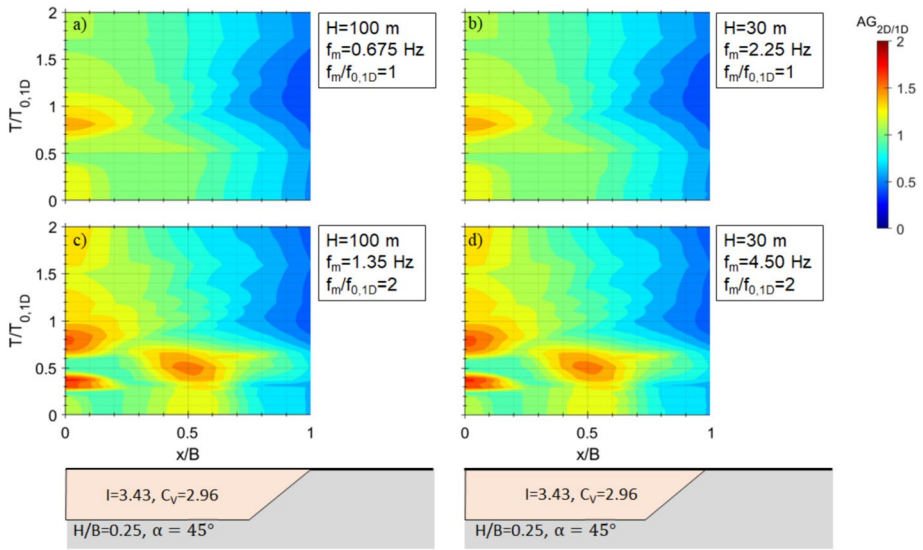
**Fig. 19** $AG_{2D/1D}$ obtained for: **a** $H = 100$ m, $f_m/f_{0,1D} = 1$; **b** $H = 30$ m, $f_m/f_{0,1D} = 1$; **c** $H = 100$ m, $f_m/f_{0,1D} = 2$; **d** $H = 30$ m, $f_m/f_{0,1D} = 2$

# 5 Valley amplification factor

The above parametric analysis on shallow valley models showed that the two-dimensional amplification results significant along most part of the alluvial soil surface, thus a valley amplification factor was defined with the aim to describe the variability of the aggravation along the valley, as a function of its geometry and mechanical properties.

For each period $T$, the mean value of $AG_{2D/1D}$ obtained from the analyses carried out adopting 12 input motions was calculated at each position $x$ along the valley surface, thus obtaining an amplification factor independent of the input frequency, as follows:

$$\overline{AG}_{2D/1D}\left(T, \frac{x}{B}\right) = \frac{1}{12} \sum_{i=1}^{12} AG_{2D/1D}\left(T_i, \frac{x}{B}\right) \tag{7}$$

The factors thus obtained were further averaged within a period range between 0 s and $T_{0,1D}$ (i.e. the resonance period of 1D soil column at the centre of the valley) and a synthetic $VAF$ was then defined as follows:

$$VAF\left(\frac{x}{B}\right) = \frac{1}{T_{0,1D}} \int_0^{T_{0,1D}} \overline{AG}_{2D/1D}\left(T, \frac{x}{B}\right) \cdot dT \tag{8}$$

The integral is calculated up to $T_{0,1D}$ because, in this range of periods the ground response seems to be more sensible to 2D effects, as shown in Figs. 9, 10 and 11 and discussed in detail in Sect. 4.1, where the spectral accelerations computed by 2D analyses at different normalised abscissae (x/B) are compared with the 1D response.

In such a way, the variation of $VAF$ along the valley can be viewed as dependent on the shape ratio, the edges slope and the impedance ratio.

In the following elaborations, only VAF values greater than or equal to unity were considered, assuming that the seismic motion at the valley surface is at least equal to that of a 1D column at the centre of the valley. This assumption makes the proposed VAF a conservative design tool, since it does not account for the attenuation that can be generated near to the edges. Figure 20a–c respectively show the influence of *H/B*, α and *I* on *VAF*, by taking as reference case the valley model with *H/B* = 0.25, α = 45° and *I* = 9.26. As shown in Fig. 20b, the *VAF* of the wedge is everywhere greater than that of any trapezoidal valley, due to the specific shape that generates peculiar wave interference phenomena. Therefore, in the following only the cases of the trapezoidal basins with α greater than 2 times the wedge slope angle will be considered. Also, the results obtained for α = 15° will not be discussed, because for *H/B* = 0.20–0.25 this edge slope is very close to that corresponding to the wedge shape, respectively equal to 11° and 14°.

The three plots show that in the central area the *VAF* increases with *H/B* and *I* and it is independent of α (except for the wedge-shaped valleys). The maximum amplification at the edge is independent of *H/B* and increases with α and *I*. Its position is strongly influenced by all the analysed factors, in particular it moves toward the centre as *H/B* and *I* increase and α decreases.

The so called 'shallow valleys' (*H/B* < 0.25) can be further distinguished into two classes based on the value of the shape ratio. If *H/B* < 0.1 they can be considered as "very shallow" basins with slight aggravation along the central sector (i.e. *VAF* lower than 1.05–1.10, depending on *I*) and gradually increasing approaching the edges. Instead, if *H/B* is greater than 0.1 but lower than the critical shape ratio (*H/B*)ₑ defined by Bard and Bouchon (1985) (see Eq. (2)), the distribution of *VAF* along the basin is characterised by two distinct peaks, one corresponding to the centre and a second one near the edges, and the valley can be classified as "moderately shallow". Table 4 summarises the influence of the different factors examined on the two-dimensional amplification along the valley.
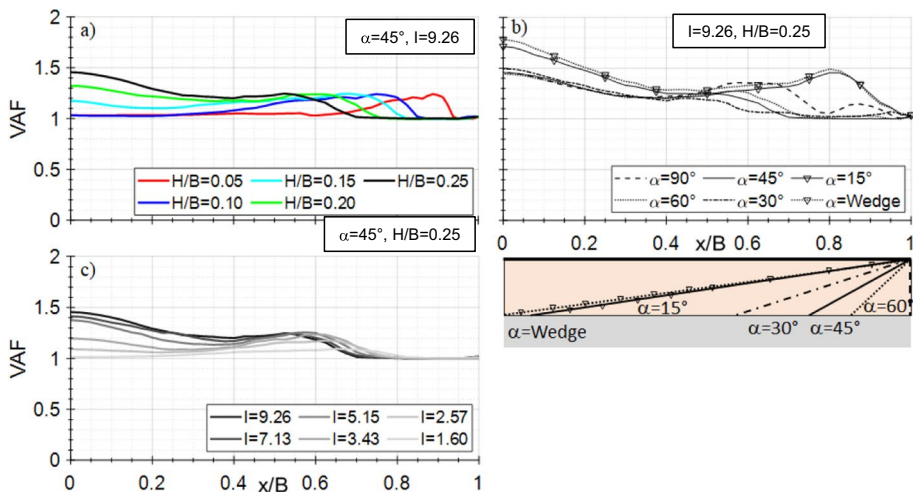


**Fig. 20** VAF obtained for variable **a** H/B; **b** α; **c** I

**Table 4** Summary of the results

| Parameter | Amplification | | Relative position of edge peak |
|---|---|---|---|
| | Centre | Edge | |
| H/B (↑ +) | (↑ +) | (=) | (→←) |
| α (↑ +) | (=) | (↑ +) | (↔) |
| I (↑ +) | (↑ +) | (↑ +) | (→←) |

*Key* (↑ +)=increase; (=)=no influence; (→←)=moves from edge to centre; (↔)=moves from centre to edge

Based on the observed trends, an analytical formulation of the *VAF* as function of the above-mentioned parameters was finally obtained.

The variation of *VAF* along the valley was approximated as the sum of two Gaussian-like functions (Fig. 21), a first one describing the amplification at the valley centre (blue curve in Fig. 21) and another one expressing its trend along the edges (red curve in Fig. 21).

The functional form proposed for analytical predictions of the *VAF* was then defined as follows:

$$VAF = 1 + (VAF(0) - 1) \cdot f_1\left(\frac{x}{B}, \frac{H}{B}, I\right) + f_2\left(\frac{x}{B}, \frac{H}{B}, I, \alpha\right) \tag{9}$$

where *VAF(0)* is the amplification computed at the middle of the valley, $f_1$ and $f_2$ the functions describing the *VAF* distributions across the central sector and along the edge, respectively. They can be expressed as:

$$VAF(0) = 1 + c_0 \cdot \left(1 - \exp\left(-\frac{(I-1)^2}{2 \cdot a_0^2}\right)\right) \tag{10}$$

$$f_1\left(\frac{x}{B}, \frac{H}{B}, I\right) = \exp\left(-\frac{\left(\frac{x}{B}\right)^2}{2 \cdot a_1^2}\right) \tag{11}$$
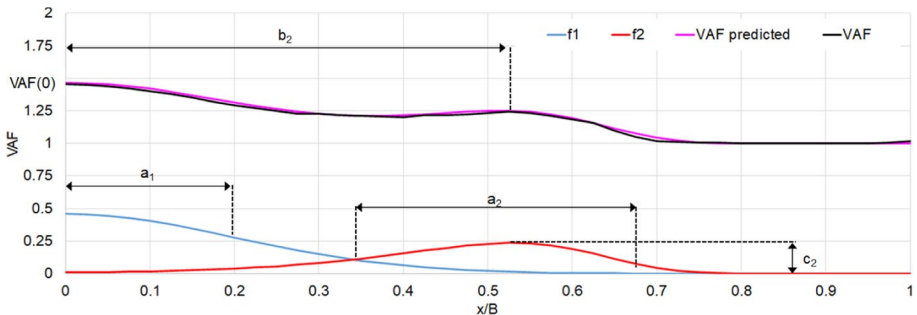


**Fig. 21** VAF model proposed in this study

$$f_2\left(\frac{x}{B},\frac{H}{B},I,\alpha\right) = c_2 \cdot \exp\left(\frac{\frac{x}{B}-b_2}{a_2} - \exp\left(\frac{\frac{x}{B}-b_2}{a_2}\right)\right) \tag{12}$$

where $c_0$, $a_0$, $a_1$, $a_2$, $b_2$ and $c_2$ are coefficients defining the Gaussian-like functions. The coefficients were preliminarily obtained by fitting the results of the numerical analyses, then their dependency on the geometrical and mechanical properties of the valley was analytically expressed. The analytical formulations of the coefficients are reported in the Appendix and in Alleanza (2022).

The five charts in Fig. 22 show the dependency of the above-described coefficients on the impedance ratio, $I$, and the shape ratio, $H/B$; in the charts, both the data points and the fitting functions are reported with symbols and curves of the same colours.

Rather than reporting $a_0$ and $c_0$, which only depend on $H/B$ (see Eqs. A.5–A.6), the aggravation factor at the valley centre, $VAF(0)$, is directly represented in Fig. 22a as an exponential function of $I$, increasing with $H/B$ and independent of $\alpha$. For a fixed geometry, $VAF(0)$ increases with $I$ up to a limit value of impedance ratio increasing with $H/B$, beyond which $VAF(0)$ remains constant.

The coefficient $a_1$ (Fig. 22b) describes the extension of the 2D aggravation sector around the centre of the valley; its value decreases with $H/B$ and $I$.
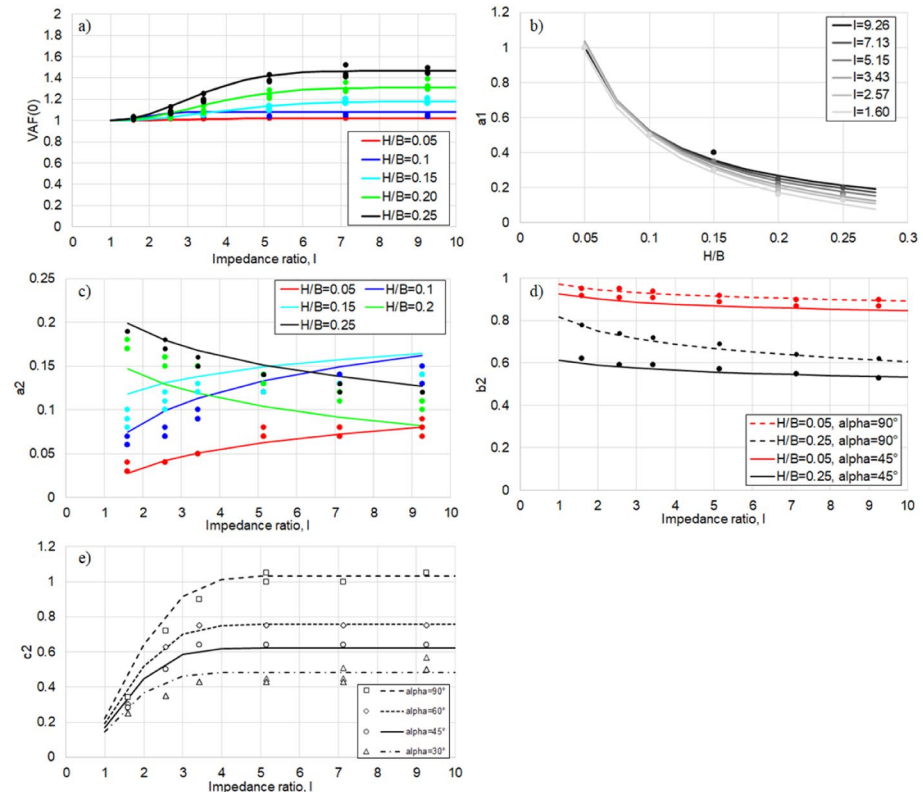


**Fig. 22** Data points and fitting functions for: **a** VAF(0); **b** a1; **c** a2; **d** b2; **e** c2

The coefficient $a_2$ (Fig. 22c) is proportional to the extension of the 2D aggravation zone at the valley edge and its dependency on *H/B* and *I* should be analysed in combination with the trend of the coefficient $a_1$. It increases with the impedance ratio for *H/B* < 0.15 and decreases in the other cases.

The coefficient $b_2$, which describes the location (Fig. 22d) of the amplification peak at the edge, depends on *H/B, I* and $\alpha$. The lateral peak of the *VAF* moves from the edge towards the middle of the valley as the impedance ratio increases for a given shape ratio, and as the *H/B* increases for a given impedance ratio.

The coefficient $c_2$ (Fig. 22e) is proportional to the amplitude of the peak of *VAF* at the edge and it is a function of *I* and $\alpha$. As for *VAF(0)*, there is a limit value of *I* beyond which this peak value remains constant, but, in this case, the maximum value of *VAF* at the edge depends on the edge slope, $\alpha$, while it is independent of *H/B*.

Summarising the above observations, the aggravation at the centre of the valley (expressed by *VAF(0)* and $a_1$) is not influenced by the slope angle, whereas the maximum amplification at the edge ($c_2$) depends on the impedance ratio *I* and $\alpha$, and its position and extension ($b_2$ and $a_2$) along the valley vary with both geometrical and mechanical parameters.

The charts in Fig. 23 compare the values of *VAF* obtained with numerical analysis (solid lines) with those predicted by the analytical functions (dashed lines): it can be noted that the latter generally overestimate the amplification because the coefficients were calibrated with a slightly over-conservative approach. This is more clearly and extensively shown by the scatter plots in Fig. 24, reporting the whole amount of the numerical data relevant to each surface node of the meshes plotted versus the corresponding analytical predictions. To better quantify how the accuracy of the proposed method in predicting the seismic motion on the surface of 2D trapezoidal valley, Fig. 25 shows the relative error for all the considered models, calculated as:
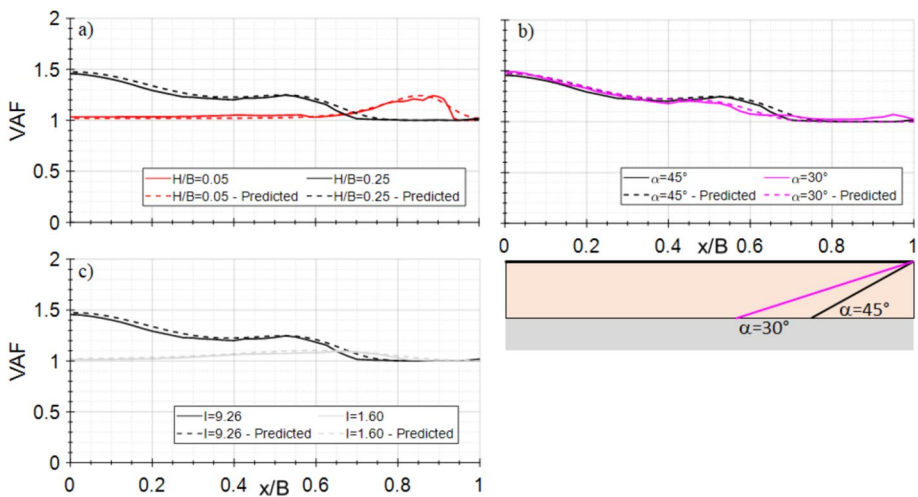


**Fig. 23** Comparison between numerical and predicted VAF for: **a** H/B = 0.05 and H/B = 0.25; **b** α = 45° and α = 30°; **c** I = 9.26 and I = 1.60
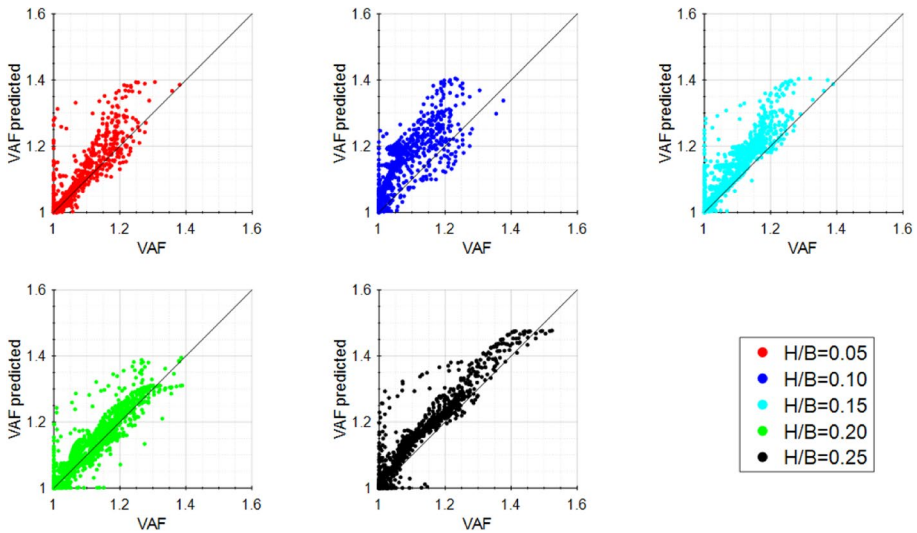
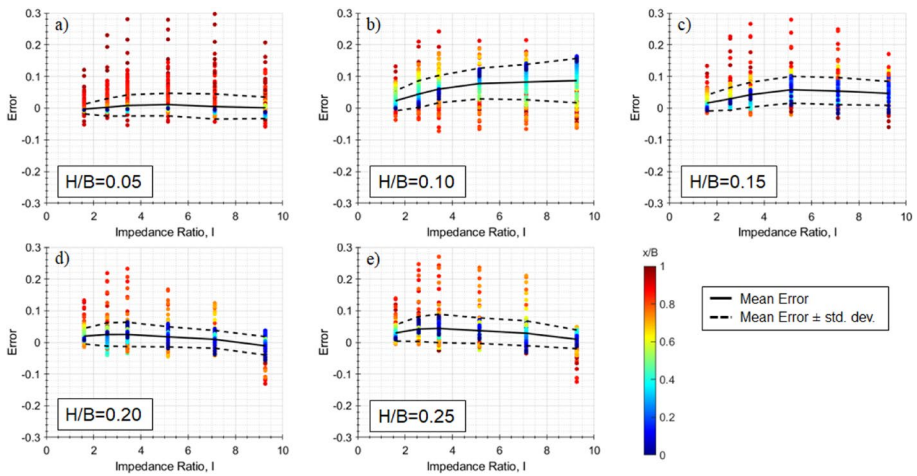**Fig. 24** Comparison between numerical and predicted VAF for all models



**Fig. 25** Relative error calculated for all models

$$Error = \frac{VAF_{predicted} - VAF_{observed}}{VAF_{observed}} \tag{13}$$

In the above expression, $VAF_{predicted}$ is calculated using the proposed Eq. (9), while $VAF_{observed}$ is the value obtained by 2D visco-elastic analyses.

In Fig. 25 the scale of colour represents the abscissa, x/B, while the solid and dashed black lines represent the mean and mean $\pm$ standard deviation relative error, respectively. The results show that the error is on average below 10% for all H/B values; moreover, the

accuracy of VAF estimation is higher in the zones where the thickness of the valley is constant (i.e. at the centre) and decreases along the edges. Finally, it can be observed that the predicted VAF is generally conservative with respect to that calculated with the numerical analyses since the coefficients in Eq. (9) were calibrated on purpose to overestimate the prediction.

The effectiveness of the proposed definition of VAF in terms of normalised parameters, already demonstrated with reference to the shape ratio H/B (see Sect. 4), was also evaluated with reference to the impedance and the frequency ratios, by carrying out additional numerical analyses. Therein, the geometric dimensions of the valley were kept constant (H = 100 m and H/B = 0.25) while the shear wave velocities of the soil and bedrock were proportionally increased, retaining the same impedance ratio (I = 3.43) as in some of the previously analysed cases. In detail, a $V_{S,r}$ value of 1200 m/s was used, which is 50% greater than that considered in the other analyses (800 m/s) and the shear wave velocity of the deformable soil was increased to 405 m/s. The input frequencies were also modified to obtain the same $f_m/f_{0,1D}$ used in the previous set of analyses.

Figure 26 shows the results of the numerical analyses in terms of VAF, obtained adopting the two couples of values of $V_S$ and $V_{S,r}$, compared with the VAF predicted with the formulas proposed in this study. The numerical values of VAF are independent of the single velocity values, if I is the same, whereas the predicted VAF slightly overestimates the numerical results, given the conservativeness of the proposed formulation.

# 6 Application of the proposed procedure

In this section, simplified evaluations of the valley amplification factor, VAF, will be applied to study the seismic response of two real valleys in Central Italy.

The first valley (Fig. 27a) consists of gravels, covered and locally interbedded by fine-grained lenses, overlying a limestone bedrock (Lemmi et al. 2017; Brunelli et al. 2019, 2021, 2022). It is located in the Italian village of Visso, situated in a highly seismically hazardous area that has experienced numerous destructive events over the centuries. The town was significantly affected by the seismic sequence that occurred in
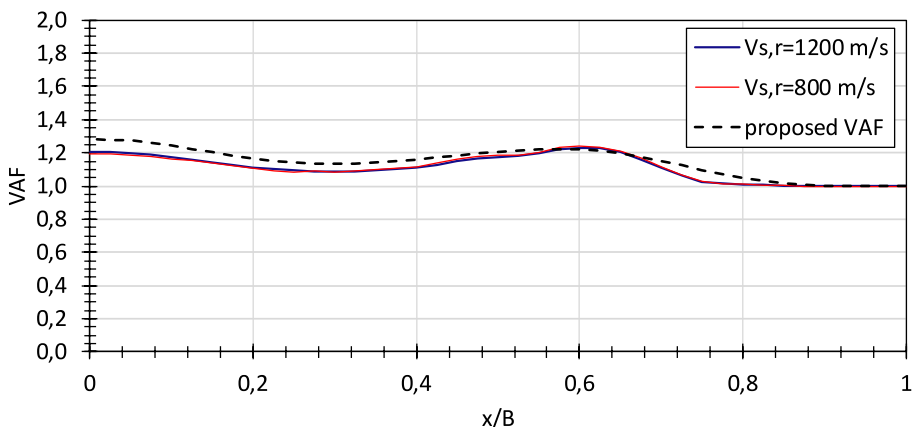


**Fig. 26** Comparison between the VAF calculated for different $V_{S,r}$ and that proposed in this study
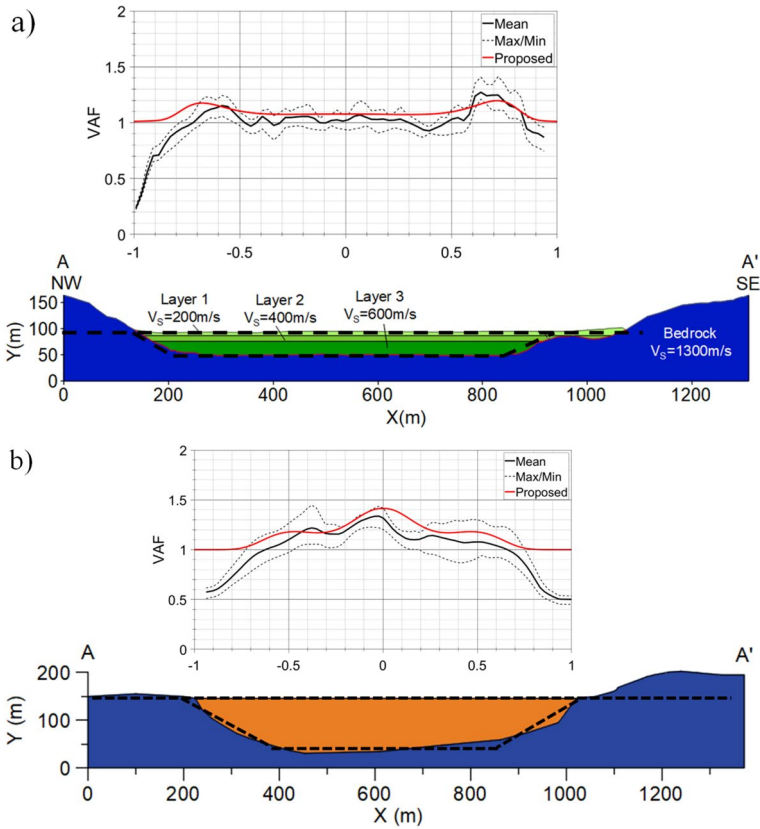
**Fig. 27** Comparison of the VAF calculated from numerical analyses and that proposed for the valleys of **a** Visso and **b** Montefranco

Central Italy since 2016, featuring several earthquakes with a moment magnitude, Mw, ranging between 5 and 6.5.

The cover deposits in the valley can be categorized into three layers with $V_S$ (shear wave velocity) increasing with depth. A shallow fine-grained layer with a thickness of 8 m and $V_S = 200$ m/s overlies a 10 m thick coarse-grained layer with $V_S = 400$ m/s, which in turn covers a 22 m succession of coarse and fine soils with a mean $V_S = 600$ m/s. This layer lies on a bedrock characterized by $V_S = 1300$ m/s. The layered soil profile has been horizontally extended to cover the entire valley, as depicted in the sections in Fig. 27a, where the green colour intensity increases with $V_S$. The interface between the bedrock and the alluvial soils is highlighted with a red line. The valley section (Fig. 27a) has a width of about 410 m, while the thickness is 40 m, resulting in a shape ratio H/B equal to 0.1. The impedance ratio, used to calculate the VAF with the proposed equation, is obtained considering a homogeneous visco-elastic model for the alluvial soil with an equivalent shear wave velocity $V_{s,eq}$ defined as:

**Table 5** Main features of the 7 accelerograms selected for Visso

| Earthquake | Date | $M_w$ | Epicentral distance (km) | Station | Site class | Component |
|---|---|---|---|---|---|---|
| Cazulas | 24/06/1984 | 4.9 | 24 | Presa de Beznar | A | N–S |
| Bingol | 01/05/2003 | 6.3 | 14 | Bingol | A | E–W |
| Lazio Abruzzo | 07/05/1984 | 5.9 | 22 | Ponte Corvo | A | N–S |
| Campano Lucano | 23/11/1980 | 6.9 | 25 | Auletta | A | N–S |
| Lazio Abruzzo | 07/05/1984 | 5.9 | 22 | Ponte Corvo | A | E–W |
| Friuli | 06/05/1976 | 6.5 | 23 | Tolmezzo | A | N–S |
| Campano Lucano | 23/11/1980 | 6.9 | 25 | Auletta | A | E–W |
| | Mean | 6.2 | 22 | | | |

**Table 6** Main features of the 7 accelerograms selected for Montefranco

| Earthquake | Date | $M_w$ | Epicentral distance (km) | Station | Site class | Component |
|---|---|---|---|---|---|---|
| Bingol | 01/05/2003 | 6.3 | 14 | Bingol | A | E–W |
| Reykjanes Peninsula | 19/03/1990 | 4.7 | 16 | Reykjavik | A | N–S |
| Izmit (aftershock) | 13/09/1999 | 5.8 | 15 | Izmit | A | N–S |
| Lazio Abruzzo (aftershock) | 11/05/1984 | 5.5 | 14 | Pescasseroli | A | N–S |
| South Iceland (aftershock) | 21/06/2000 | 6.4 | 6 | Selfoss | A | N–S |
| South Iceland (aftershock) | 21/06/2000 | 6.4 | 15 | Hella | A | E–W |
| South Iceland | 17/06/2000 | 6.5 | 5 | Selfoss | A | E–W |
| | Mean | 5.9 | 12 | | | |

$$V_{S,eq} = \frac{H}{\sum_{i=1}^{n} \frac{h_i}{V_{S,i}}} \tag{14}$$

with H the total thickness of the soil deposit at the centre of the valley, $h_i$ and $V_{S,i}$ the height and shear wave velocity of the i-th layer and n the number of the layers. Therefore the $V_{S,eq}$ is equal to 470 m/s and $\gamma = 20$ kN/m$^3$, while for the bedrock $V_S = 1300$ m/s and $\gamma = 22$ kN/m$^3$, thus the impedance ratio is about 3.

The second valley (Fig. 27b), located in Montefranco (Faralli et al. 2018), has a maximum thickness of about 110 m and a width of approximately 850 m. It is predominantly filled with fine-grained soil, resulting in a shape ratio of about 0.26. The soil is nearly homogeneous with $V_S = 260$ m/s and $\gamma = 18$ kN/m$^3$, and the bedrock has $V_S = 850$ m/s and $\gamma = 23$ kN/m$^3$, yielding an impedance ratio of 4.2.

For both valleys, 2D visco-elastic dynamic analyses were conducted using FLAC adopting the actual Vs profiles of the valleys. In these analyses, seven natural accelerograms were applied, selected to ensure that the mean response spectrum aligns with the reference one prescribed by the Italian national building code at life limit state (SLV) for the respective sites. Tables 5 and 6 show the main properties of the selected signals while the Figs. 28a and 29a show the comparison among the response spectra of the seven selected accelerograms, the average spectrum and the one defined by NTC (2018)
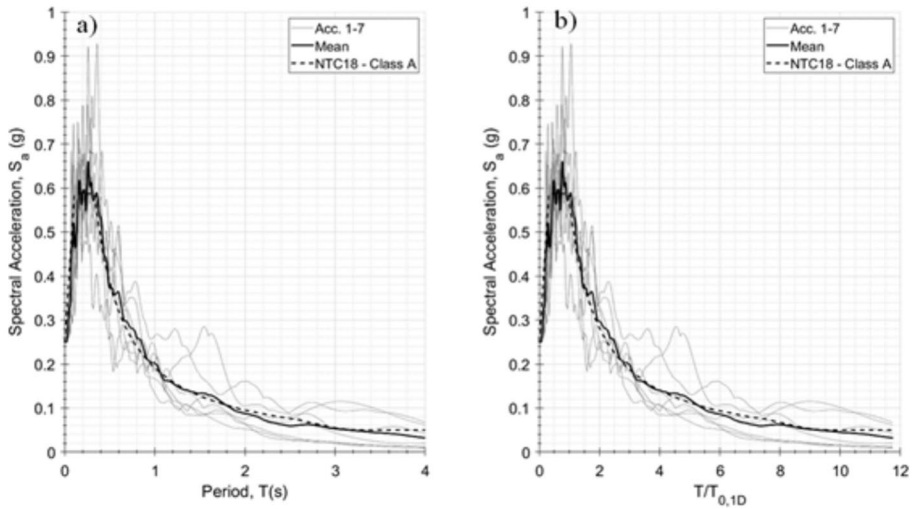
**Fig. 28** **a** Comparison among the response spectra of the 7 input selected for Visso, the average spectrum, and the one defined by NTC (2018); **b** the same spectra plotted as a function of the normalised period
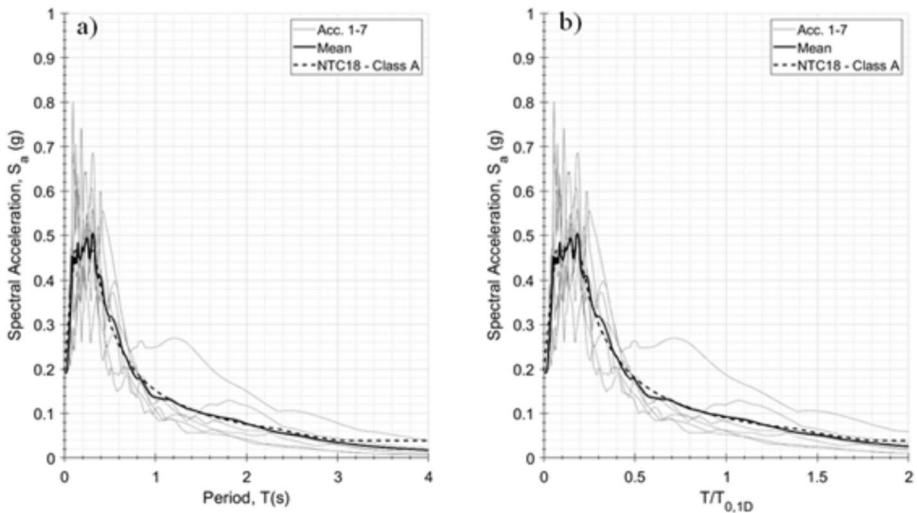


**Fig. 29** **a** Comparison among the response spectra of the 7 input selected for Montefranco, the average spectrum and the one defined by NTC (2018); **b** the same spectra plotted as a function of the normalised period

for class A for Visso and Montefranco, respectively. In Figs. 28b and 29b, the same spectra are shown but with the periods scaled with respect to $T_{0,1D}$.

The accelerograms computed at the ground surface were processed to calculate the Valley Amplification Factor (VAF) for each surface point. It's important to note that the reference 1D vertical is that of the centre valley of each section. Figure 27a and b

shows the comparison between the VAF calculated with the numerical analyses and that obtained with the equations proposed in this study.

In the case of Visso (Fig. 27a), where the valley is very shallow (H/B = 0.1), the average VAF of the seven accelerograms is slightly higher than 1 at the centre of the valley. At the edges, it increases to about 1.3. The trend differs on the two sides of the valley because, on the right, the valley is located at the foot of a slope, while on the left, the surface is almost horizontal. The VAF obtained with the proposed equations (red line) is generally close to the mean VAF, except on the left edge where strong geometric effects, not fully captured by the simplified model, come into play.

In the case of Montefranco (Fig. 27b), where the valley is shallow (H/B = 0.26), the mean VAF calculated for the seven accelerograms is approximately 1.3 at the centre and 1.1–1.2 at the edges. Similar to the Visso case, the VAF computed with the proposed
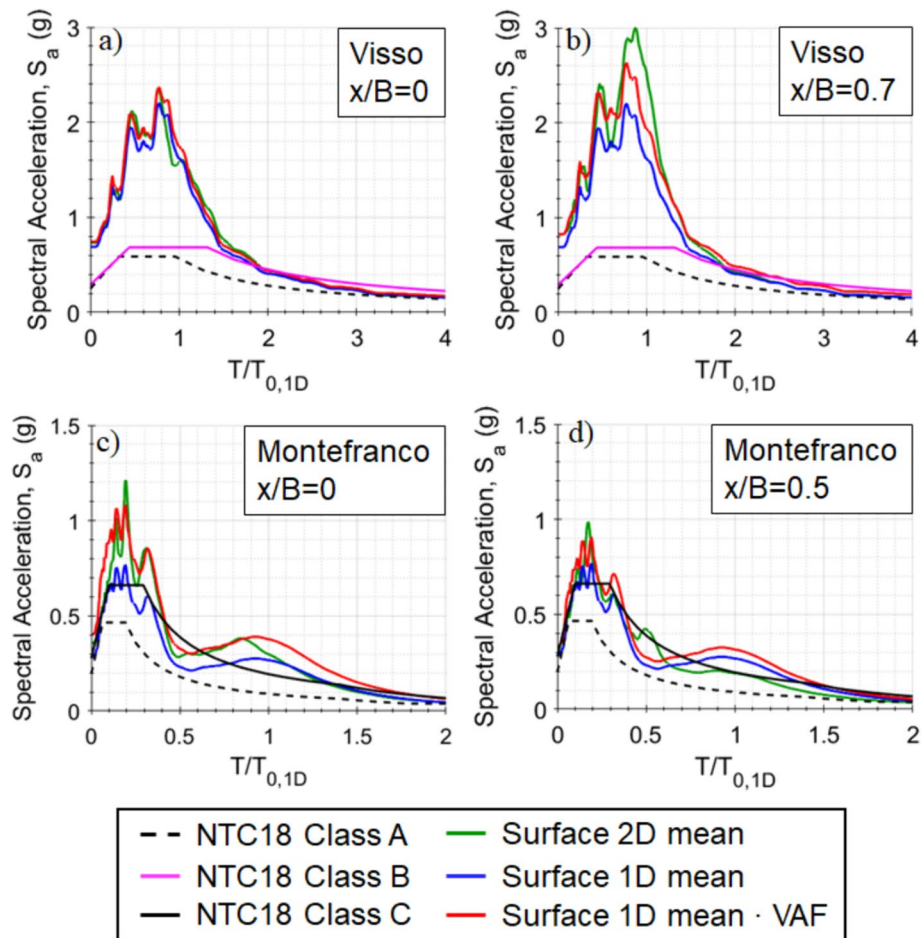


Fig. 30 Comparison between spectra calculated at the centre and edge for **a, b** Visso and **c, d** Montefranco valley with: 2D visco-elastic analyses (green line); 1D visco-elastic analyses at the centre (blue line); 1D amplify with the proposed VAF (red line); Italian National code for soil class A (dashed black line), B (magenta line) and C (black line)

equations (red line) closely aligns with the mean value for most of the valley, generally falling between the minimum and maximum values.

Finally, Fig. 30 shows a comparison among the mean response spectra calculated by:

- 2D analyses at the centre and at the edge for the Visso (a,b) and Montefranco (c,d) valleys (green lines);
- 1D analyses carried out along the vertical at the centre valley (blue lines);
- amplifying the 1D spectra of the centre valley with the proposed VAF (red lines).

The spectra specified by the Italian technical standards for soil classes A, B and C (dashed black line, solid black line and pink lines) are also plotted for reference.

The results highlight that, in the centre of both valleys the proposed VAF leads to a better estimate of the 2D amplification, while in the zone close to the edges it is less capable of predicting the expected surface seismic motion, because of the significant variability of the 1D frequency response in this zone. However, on average, the suggested approach enables to estimate surface spectra closer to those predicted by 2D analyses with respect to that obtained with 1D analysis.

## 7 Conclusions

This paper presents the outcomes of extensive parametric numerical analyses investigating the seismic response of 2D symmetrical homogeneous alluvial basins. The study aims to investigate the influence of both geometric and mechanical parameters on amplification along the valley. Authors selected some dimensionless parameters to describe both the geometry and the mechanical characteristics of the valleys. The key findings underscore the predominant role of the shape ratio (H/B). For very shallow valleys (H/B < 0.1), 2D amplification occurs near the edges, while the central part is primarily affected by stratigraphic effects. As H/B increases, 2D effects become significant across the entire basin, categorizing the valley as "moderately shallow." The aggravation factor exhibits two peaks, one in the valley's middle and another at the edge. The effectiveness of the selected dimensionless parameters and the generality and sufficiency of the performed analyses were also verified.

The results obtained can be considered as reliable for the so-called 'shallow valleys', i.e. those characterised by H/B < 0.3. They are expected to be extended to the 'deep valley' cases, with a specifically designed parametric study.

The study further synthesizes numerical results to propose an analytical equation for the Valley Amplification Factor (VAF). This equation considers shape ratio, edge slope, and impedance ratio, offering a tool for preliminary estimation of 2D effects in the case of shallow valleys approximated to a trapezoidal shape, without requiring detailed numerical analysis.

It has been conceived to furnish provide a simple, and effective, but yet a conservative estimation. As a matter of fact, the VAF defined in this study is taken as always greater than 1. This simplified assumption could lead to a non-realistic prediction of the motion at the edge of the valleys, where the destructive interference between reflected, refracted and surface waves could result in a de-amplification of the ground motion. Therefore, the VAF, as defined in this study, is reasonably suitable for shallow trapezoidal valleys (H/B < 0.25–0.3), homogeneous and visco-elastic, except for the limited zones near the edges. Furthermore, the definition of

a unique VAF value uniformly increasing the spectral ordinates is an effective straightforward practice-oriented simplified quantification of valley effects, but again it leads to a conservative estimation of spectral ordinates at high periods, since valley effects primarily affect the high high-frequency components of the seismic ground motion. Finally, it is worth highlighting that the proposed VAF can be more reliably adopted with reference to low- to medium-amplitude seismic ground motions, for which non-linearity is not strongly mobilised.

Comparison with 2D visco-elastic analysis for two real valleys in Central Italy, representing very shallow and moderately shallow cases, reveals that the proposed VAF closely aligns with average VAF values obtained from natural accelerograms. Notably, the proposed equation captures key aspects, demonstrating its utility in seismic microzonation studies.

The suggested VAF equation could potentially serve as a reference in defining a coefficient for incorporation into national seismic codes of practice and Eurocode 8 (2004). In other words, VAF might express in-depth morphological amplification in a similar way as the well-known topographic amplification factor, often termed as TAF or $S_T$, as frequently adopted in the above-mentioned standards.

Additionally, it lays the groundwork for future research to refine simplifying assumptions employed in the proposed equation. As a matter of fact, the effects of heterogeneity and non-linearity that are not included in this study will be object of future research.

## Appendix

$$VAF = 1 + (VAF(0) - 1) \cdot f_1\left(\frac{x}{B}, \frac{H}{B}, I\right) + f_2\left(\frac{x}{B}, \frac{H}{B}, I, \alpha\right) \tag{A.1}$$

$$f_1\left(\frac{x}{B}, \frac{H}{B}, I\right) = \exp\left(-\frac{\left(\frac{x}{B}\right)^2}{2 \cdot a_1^2}\right) \tag{A.2}$$

$$f_2\left(\frac{x}{B}, \frac{H}{B}, I, \alpha\right) = c_2 \cdot \exp\left(\frac{\frac{x}{B} - b_2}{a_2} - \exp\left(\frac{\frac{x}{B} - b_2}{a_2}\right)\right) \tag{A.3}$$

$$VAF(0) = 1 + c_0 \cdot \left(1 - \exp\left(-\frac{(I-1)^2}{2 \cdot a_0^2}\right)\right) \tag{A.4}$$

$$a_0 = \begin{cases} \frac{H}{B} < 0.10 & 2.463 - 16.509 \cdot \frac{H}{B} \\ 0.10 \le \frac{H}{B} < 0.15 & 32.838 \cdot \frac{H}{B} - 2.472 \\ \frac{H}{B} \ge 0.15 & 0.153.290 - 5.574 \cdot \frac{H}{B} \end{cases} \tag{A.5}$$

$$c_0 = 2.350 \cdot \left(1 - \exp\left(-\frac{\left(\frac{H}{B}\right)^2}{0.282}\right)\right) \tag{A.6}$$

$$a_1 = x_1 \cdot \left(\frac{H}{B}\right)^{x_2} + x_3 \tag{A.7}$$

$$a_2 = x_4 + \ln\left(I^{x_5}\right) \tag{A.8}$$

$$b_2 = x_6 + \ln\left(I^{-x_7}\right) \tag{A.9}$$

$$c_2 = x_{12} \cdot \left(1 - \exp\left(-\frac{I^2}{2 \cdot x_{13}^2}\right)\right) \tag{A.10}$$

$$x_1 = 0.204 \cdot I^{-0.409} - 0.00998 \tag{A.11}$$

$$x_2 = 0.531 \cdot I^{-0.303} - 1.160 \tag{A.12}$$

$$x_3 = -4.495 \cdot I^{-0.0372} + 4.103 \tag{A.13}$$

$$x_4 = 0.335 \cdot \left(1 - \exp\left(-\frac{\left(\frac{H}{B}\right)^2}{2 \cdot 0.172^2}\right)\right) \tag{A.14}$$

$$x_5 = \begin{cases} \forall \frac{H}{B} \le 0.15 \rightarrow -8.567 \cdot \left(\frac{H}{B}\right)^2 + 1.679 \cdot \frac{H}{B} - 0.0327 \\ \forall \frac{H}{B} > 0.15 \rightarrow 1.173 \cdot 10^{-9} \cdot \left(\frac{H}{B}\right)^{-9.421} - 0.0414 \end{cases} \tag{A.15}$$

$$x_6 = x_8 + \ln\left(\alpha^{x_9}\right) \tag{A.16}$$

$$x_7 = \begin{cases} \forall \frac{H}{B} < 0.10 \rightarrow -0.0042 + 0.764 \cdot \frac{H}{B} \\ \forall \frac{H}{B} \ge 0.10 \rightarrow x_{10} + \ln\left(\alpha^{x_{11}}\right) \end{cases} \tag{A.17}$$

$$x_8 = 0.967 - 5.849 \cdot \frac{H}{B} \tag{A.18}$$

$$x_9 = 0.0097 + 1.127 \cdot \frac{H}{B} \tag{A.19}$$

$$x_{10} = -0.375 \cdot \ln\left(\frac{H}{B}\right) - 0.793 \tag{A.20}$$

$$x_{11} = 0.088 \cdot \ln\left(\frac{H}{B}\right) + 0.203 \tag{A.21}$$

$$x_{12} = 0.207 + 0.00919 \cdot \alpha \tag{A.22}$$

$$x_{13} = 1.064 + 0.00416 \cdot \alpha \tag{A.23}$$

## Declarations

**Conflict of interest** The authors declare that they have no known competing financial interests or personal relationships that could have appeared to influence the work reported in this paper.

## References

Aki K (1988) Local site effects on strong ground motion. In: Van Thun, JL (ed) Earthquake engineering and soil dynamics II-recent advances in ground motion evaluation, pp 103–155

Alleanza GA (2022) Study of the seismic response of alluvial valleys. Doctoral dissertation, University of Napoli Federico II, Napoli, Italy. http://www.fedoa.unina.it/id/eprint/14488

Alleanza GA, Chiaradonna A (2018) Previsione degli effetti di non linearità dei terreni: confronto tra codici di calcolo per analisi 1D di risposta sismica locale. In: Proceedings of the 8th Incontro Annuale Giovani Ingegneri Geotecnici, Udine (in Italian)

Alleanza GA, d'Onofrio A, Silvestri F (2019a) Seismic microzonation of an alluvial valley hit by the 2016 Central Italy earthquake. In: Earthquake geotechnical engineering for protection and development of environment and constructions: proceedings of the 7th international conference on earthquake geotechnical engineering, (ICEGE 2019): 1074–1081. ISBN 978-0-367-14328-2

Alleanza GA, Chiaradonna A, d'Onofrio A, Silvestri F (2019b) Parametric study on 2D effect on the seismic response of alluvial valleys. In: Earthquake geotechnical engineering for protection and development of environment and constructions: proceedings of the 7th international conference on earthquake geotechnical engineering, (ICEGE 2019): 1082–1089. ISBN 978-0-367-14328-2

Bard PY, Bouchon M (1980a) The seismic response of sediment-filled valleys. Part 1. The case of incident SH waves. Bull Seismol Soc Am 70(4):1263–1286

Bard PY, Bouchon M (1980b) The seismic response of sediment-filled valleys. Part 2. The case of incident P and SV waves. Bull Seismol Soc Am 70(5):1921–1941

Bard PY, Bouchon M (1985) The two-dimensional resonance of sediment-filled valleys. Bull Seismol Soc Am 75(2):519–541

Bard PY, Gariel JC (1986) Seismic response of two-dimensional sedimentary deposits with large vertical velocity gradients. Bull Seismol Soc Am 76(2):343–366

Bielak J, Xu J, Ghattas O (1999) Earthquake ground motion and structural response in alluvial valleys. J Geotech Geoenviron Eng 125:413–423

Bouckovalas GD, Papadimitriou AG (2005) Numerical evaluation of slope topography effects on seismic ground motion. Soil Dyn Earthq Eng 25:547–558

Boudghene-Stambouli A, Bard P-Y, Chaljub E, Moczo P, Kristek J, Stripajova S, Durand C, Zendagui D, Derras B (2018) 2D/1D aggravation factors: from a comprehensive parameter study to simple estimates with a neural network model. In: 16ECEE (16th European conference on earthquake engineering), Thessaloniki, Greece, June 18–21, 2018, paper #624, p 12

Bray JD (2007) Simplified seismic slope displacement procedures. In: Pitilakis KD (ed) Earthquake geotechnical engineering—proceedings IV ICEGE (Invited Lectures), Thessaloniki, vol 6. pp 327–353

Brunelli A, Sivori D, Cattari S, Piro A, de Silva F, Parisi F, Sica S, Silvestri F (2019) Soil-structure interaction effects on the dynamic behaviour of a masonry school damaged by the 2016–2017 Central Italy earthquake sequence. In: Silvestri F, Moraci N (eds) Earthquake geotechnical engineering for protection and development of environment and constructions, proceedings of the VII international conference on earthquake geotechnical engineering, pp 1655–1663

Brunelli A, de Silva F, Piro A, Parisi F, Sica S, Silvestri F, Cattari S (2021) Numerical simulation of the seismic response and soil–structure interaction for a monitored masonry school building damaged by the 2016 Central Italy earthquake. Bull Earthq Eng 19(2):1181–1211. https://doi.org/10.1007/s10518-020-00980-3

Brunelli A, Alleanza GA, Cattari S, de Silva F, d'Onofrio A (2022) Simulation of damage observed on buildings in aggregate after the 2016–2017 Central Italy earthquake accounting for site effects and soil-structure interaction. In: Proceedings of the 3rd international symposium on geotechnical engineering for the preservation of monuments and historic sites, Napoli 2022

Capatti MC, Tropeano G, Morici M, Carbonari S, Dezi F, Leoni G, Silvestri F (2017) Implications of non-synchronous excitation induced by nonlinear site amplification and soil-structure interaction on the seismic response of multi-span bridges founded on piles. Bull Earthq Eng 15(11):4963–4995. https://doi.org/10.1007/s10518-017-0165-z

Chávez-García FJ, Faccioli E (2000) Complex site effects and building codes: making the leap. J Seismolog 4(1):23–40

Chiarini M, d'Onofrio A, Evangelista L, Penna A, Silvestri F (2011). The role of site effects and near-source seismic actions on ground and buildings response at some sites across the Aterno river valley (Italy). In: 5th International conference on earthquake geotechnical engineering—10–13 Gennaio 2011—Santiago-Chile

Costanzo A, d'Onofrio A, Silvestri F (2019) Seismic response of a geological, historical and architectural site: the Gerace cliff (southern Italy). Bull Eng Geol Env 78(8):5617–5633

Dakoulas P, Gazetas G (1985) A class of inhomogeneous shear models for seismic response of dams and embankments. Int J Soil Dyn Earthq Eng 4(4):166–182

De Crescenzo M, Evangelista L, Lanzano G, Puglia R, d'Onofrio A, Silvestri F (2018) Seismic characterization of the accelerometric stations along an array in the Sulmona basin. In: Proceedings of the 16th European conference on Earthquake Engineering—Tessaloniki

d'Onofrio A, Silvestri F (2001) Influence of micro-structure on small-strain stiffness and damping of fine grained soil and effects on local site response. In: International conferences on recent advances in geotechnical earthquake engineering and soil dynamics, p 15

Eurocode 8. (2004) Eurocode 8: design of structures for earthquake resistance—Part 1: general rules, seismic actions and rules for buildings. https://doi.org/10.1680/cien.144.6.55.40618

Faccioli E, Vanini M, Frassine L (2002) "Complex" site effects in earthquake ground motion, including topography. In: Proceedings of the 12th European conference on Earthquake Engineering, p 844

Faralli L, Gasparri N, Piccioni R, Venanti LD (2018) Microzonazione Sismica di Livello 3 del Comune di Montefranco ai sensi dell'Ordinanza del Commissario Straordinario n.24 registrata il 15 maggio 2017 al n. 1065

Gao S, Liu H, Davis PM, Knopoff L (1996) Localized amplification of seismic waves and correlation with damage due to the Northridge earthquake: evidence for focusing in Santa Monica. Bull Seismol Soc Am 86B:S209–S230

Garini E, Anastasopoulos I, Gazetas G (2020) Soil, basin and soil-building-soil interaction effects on motions of Mexico City during seven earthquakes. Geotechnique 70(7):581–607

Gelagoti F, Kourkoulis R, Anastasopoulos I, Tazoh T, Gazetas G (2010) Seismic wave propagation in a very soft alluvial valley: sensitivity to ground motion details and soil nonlinearity, and generation of a parasitic vertical component. Bull Seismol Soc Am 100(6):3035–3054

Gelagoti F, Kourkoulis R, Anastasopoulos I, Gazetas G (2012) Nonlinear dimensional analysis of trapezoidal valleys subjected to vertically propagating SV waves. Bull Seismol Soc Am 102(3):999–1017

Itasca Consulting Group, Inc. (2016) FLAC—Fast Lagrangian Analysis of Continua, Ver. 8.0. Minneapolis: Itasca

Iyisan R, Khanbabazadeh H (2013) A numerical study on the basin edge effect on soil amplification. Bull Earthq Eng 11:1305–1323

Kottke AR, Rathje EM (2008) Technical manual for Strata, Report No.: 2008/10. Pacific Earthquake Engineering Research Centre, University of California, Berkeley

Kristek J, Moczo P, Bard P-Y, Hollender F, Stripajová S (2018) Computation of amplification factor of earthquake ground motion for a local sedimentary structure. Bull Earthq Eng 16(6):2451–2475. https://doi.org/10.1007/s10518-018-0358-0

Kuhlemeyer RL, Lysmer J (1973) Finite element method accuracy for wave propagation problems. Soil Mech Found 99(5):421–427

Lanzo G, Silvestri F, Costanzo A, d'Onofrio A, Martelli L, Pagliaroli A, Sica S, Simonelli AL (2011) Site response studies and seismic microzoning in the Middle Aterno valley (L'Aquila, Central Italy). Bull Earthq Eng 9(5):1417–1442

Lemmi M, Lolli O, Zeni S (2017) Microzonazione Sismica di Livello 3 del Comune di Visso ai sensi dell'Ordinanza del Commissario Straordinario n.24 registrata il 15 maggio 2017 al n. 1065. https://sisma2016data.it/microzonazione/

Makra K, Chávez-García FJ, Raptakis D, Pitilakis K (2005) Parametric analysis of the seismic response of a 2D sedimentary valley: implications for code implementations of complex site effects. Soil Dyn Earthq Eng 25(4):303–315. https://doi.org/10.1016/j.soildyn.2005.02.003

Moczo P, Kristek J, Bard P-Y, Stripajová S, Hollender F, Chovanová Z, Kristeková M, Sicilia D (2018) Key structural parameters affecting earthquake ground motion in 2D and 3D sedimentary structures. Bull Earthq Eng 16(6):2421–2450. https://doi.org/10.1007/s10518-018-0345-5

NTC (2018) Ministero delle infrastrutture e dei trasporti. D.M. 17/01/2018. Aggiornamento delle norme tecniche per le costruzioni. S.O. n. 8 alla Gazzetta Ufficiale della Repubblica Italiana, n. 42 del 20 Febbraio 2018 (in Italian)

Pagliaroli A, Lanzo G, D'Elia B, Costanzo A, Silvestri F (2007) Topographic amplification factors associated to cliff morphology: numerical results from two case studies in Southern Italy and comparison with EC8 recommendations. In: Workshop on 'Evaluation Committee for the Application of EC8', XIV ECSMGE, Madrid

Pagliaroli A, Pergalani F, Ciancimino A, Chiaradonna A, Compagnoni M, de Silva F, Foti S, Giallini S, Lanzo G, Lombardi F, Luzi L, Macerola L (2020) Site response analyses for complex geological and morphological conditions: relevant case-histories from 3rd level seismic microzonation in Central Italy. Bull Earthq Eng 18(2):5741–5777

Paolucci R (1999) Fundamental vibration frequencyes of 2D geological structures. In: Proceedings of 2nd international conference on earthquake geotechnical engineering, Lisbon, vol 1. p 255-260

Paolucci R (2002) Amplification of earthquake ground motion by steep topographic irregularities. Earthq Eng Struct Dynam 31:1831–1853

Papadimitriou AG (2019) An engineering perspective on topography and valley effects on seismic ground motion. Earthquake geotechnical engineering for protection and development of environment and constructions: In: Proceedings of the 7th international conference on earthquake geotechnical engineering, (ICEGE 2019): 426–441. ISBN 978-0-367-14328-2

Papadimitriou AG, Paraskevopoulos SA, Lamprakopoulos AN (2018) Aggravation of spectral acceleration along 2D symmetrical trapezoidal valleys. In: Proceedings, 16th European conference on earthquake engineering paper ID, p 11491

Pitarka A, Irikura K, Iwata T, Takao T (1996) Basin structure effects in the Kobe area inferred from the modeling of ground motions from two aftershocks of the January 17 1995, Hyogo-ken Nanbu earthquake. J Phys Earth 44:563–576

Pitilakis K, Riga E, Anastasiadis A, Fotopoulou S, Karafagka S (2019) Towards the revision of EC8: proposal for an alternative site classification scheme and associated intensity dependent spectral amplification factors. Soil Dyn Earthq Eng. https://doi.org/10.1016/j.soildyn.2018.03.030

Psarropoulos PN, Tazoh T, Gazetas G, Apostolu M (2007) Linear and non linear valley amplification effects on seismic ground motion. Soils Found 47(5):857–871

Riga E, Makra K, Pitilakis K (2016) Aggravation factors for seismic response of sedimentary basins: a code-oriented parametric study. Soil Dyn Earthq Eng 91:116–132

Riga E, Makra K, Pitilakis K (2018) Investigation of the effects of sediments inhomogeneity and nonlinearity on aggravation factors for sedimentary basins. Soil Dyn Earthq Eng 110:284–299

Sanchez-Sesma FJ, Chavez-Garcia F, Bravo MA (1988) Seismic response of a class of alluvial valley for incident SH waves. Bull Seismol Soc Am 78(1):83–95

Sgattoni G, Castellaro S (2020) Detecting 1-D and 2-D ground resonances with a single-station approach. Geophys J Int 223:471–487

Sgattoni G, Lattanzi G, Castellaro S (2019) 2D resonance detected with H/V measurements. In: Proceedings of the 38th Convegno Nazionale del Gruppo Nazionale di Geofisica della Terra Solida, p 470–475

Tropeano G, Soccodato FM, Silvestri F (2018) Re-evaluation of code-specified stratigraphic amplification factors based on Italian experimental records and numerical seismic response analyses. Soil Dyn Earthq Eng 110:262–275. https://doi.org/10.1016/j.soildyn.2017.12.030

Uzielli M, Facciorusso J, Madiai C (2022) Statistical calibration of two-dimensional seismic aggravation effects for homogeneous basins. Soil Dyn Earthq Eng 2022(163):107533

Verrucci L, Pagliaroli A, Lanzo G, di Buccio F, Biasco AP, Cucci C (2022) Damping formulations for finite difference linear dynamic analyses: performance and practical recommendations. Comput Geotech. https://doi.org/10.1016/j.compgeo.2021.104568

Vessia G, Russo S, Lo Presti D (2011) A new proposal for the evaluation of the amplification coefficient due to valley effects in the simplified local seismic response analyses. Riv Ital Geotec 4:51–77

Zhu C, Thambiratnam D (2016) Interaction of geometry and mechanical property of trapezoidal sedimentary basins with incident SH waves. Bull Earthq Eng 14(11):2977–3002

Zhu C, Chávez-García FJ, Thambiratnam D, Gallage C (2018a) Quantifying the edge-induced seismic aggravation in shallow basins relative to the 1D SH modelling. Soil Dyn Earthq Eng 115:402–412

Zhu C, Riga E, Pitilakis K, Zhang J, Thambiratnam D (2018b) Seismic aggravation in shallow basins in addition to one-dimensional site amplification. J Earthq Eng. https://doi.org/10.1080/13632469.2018.1472679

Zhu C, Thambiratnam D, Gallage C (2018c) Statistical analysis of the additional amplification in deep basins relative to the 1D approach. Soil Dyn Earthq Eng 104:296–306